ADVANCED ENERGY MATERIALS
www.advenergymat.de

Reticulated Porous Perovskite Structures for Thermochemical Solar Energy Storage

Mathias Pein, Luca Matzel, Lamark de Oliveira, Gözde Alkan, Alexander Francke, Peter Mechnich, Christos Agrafiotis,* Martin Roeb, and Christian Sattler*

The inherent capability of concentrated solar power (CSP) plants for sensible thermal energy storage ensures their continuous operation and is considered their most crucial competitive edge versus other renewable energy sources. The storage density of air-operated CSP plants can be significantly increased by hybridizing sensible with thermochemical storage of solar heat, exploiting reversible air–solid oxide reduction–oxidation reactions. Thermochemical storage-relevant-protocols testing of in-house manufactured lab-scale reticulated porous ceramic foams made entirely of $CaMnO_3$ perovskite reveals fully reversible reduction-oxidation in up to 46 cycles between 300 and 1100 °C under air, without any deterioration of the foams' structural integrity and exploitable endothermic/exothermic heat effects between 890 and 920 °C linked to an orthorhombic-to-cubic phase transition. Dilatometry experiments with $CaMnO_3$ bars under identical cyclic conditions demonstrate the correlation of this phase transition to an increase in the thermal expansion coefficient but nevertheless, complete recovery of the initial specimen dimensions upon completion of a full heat-up/cooldown redox cycle. The possibility of shaping into sturdy reticulated porous ceramic structures which exhibit complete dimensional reversibility upon cyclic redox operation, combined with the low cost, earth abundance and environmentally benign character of the constituting elements, render such perovskite compositions extremely attractive for the manufacture of large-scale porous structured objects for exploitation in various thermochemical processes.

1. Introduction

Concentrated solar power (CSP) systems convert solar energy to medium- to high-temperature heat and through that to electricity. In contrast to photovoltaics and wind turbines where solar/wind energy is converted directly to electrical power needing immediate supply to the grid, heat can be stored for long periods and supplied on demand. Through this inherent capability, CSP plants can play a crucial role on our transition from our current fossil fuels-based energy system to one based to a large extent on fluctuating power from renewable energy sources, being able to supply cost-effective, base-load and peak-load electricity and stabilizing the power grids. The approach set forth herein is targeted on increasing the storage density of air-operated CSP plants by hybridizing sensible with thermochemical storage of solar heat within the same storage unit volume, through the exploitation of reversible reduction-oxidation reactions of air in direct contact with porous ceramic structures made entirely of earth-abundant, inexpensive, nontoxic metal oxides. This approach is entirely compatible with the "modularity" and thus straightforward scalability of current state-of-the-art regenerative sensible heat storage/recovery systems that are manufactured from similar, yet chemically inert inexpensive porous structures like bricks and honeycombs.

Historically, coupling redox (reduction-oxidation) chemistries operating on the transition between the oxidized (MeO_x) and the reduced state ($MeO_{x-\delta}$) of a metal oxide exhibiting multiple

M. Pein, L. Matzel, L. Oliveira, C. Agrafiotis, M. Roeb, C. Sattler
DLR - Deutsches Zentrum für Luft- und Raumfahrt e.V./German Aerospace Center - Institute of Future Fuels
Linder Höhe
51147 Cologne, Germany
E-mail: mathias.pein@dlr.de; christos.agrafiotis@dlr.de

The ORCID identification number(s) for the author(s) of this article can be found under https://doi.org/10.1002/aenm.202102882.

© 2022 The Authors. Advanced Energy Materials published by Wiley-VCH GmbH. This is an open access article under the terms of the Creative Commons Attribution License, which permits use, distribution and reproduction in any medium, provided the original work is properly cited.

DOI: 10.1002/aenm.202102882

M. Pein, C. Sattler
TU Dresden
Faculty of Mechanical Science and Engineering
Institute of Power Engineering
Solar Fuel Production
01062 Dresden, Germany

G. Alkan, A. Francke, P. Mechnich
DLR - Deutsches Zentrum für Luft- und Raumfahrt e.V./German Aerospace Center - Institute of Materials Research
Linder Höhe
51147 Cologne, Germany

Check for updates
16146840, 2022, 10, Downloaded from https://onlinelibrary.wiley.com/doi/10.1002/aenm.202102882 by Dtsch Zentrum F. Luft-U. Raum Fahrt In D. Helmholtz Gemein., Wiley Online Library on [05/12/2022]. See the Terms and Conditions (https://onlinelibrary.wiley.com/terms-and-conditions) on Wiley Online Library for rules of use; OA articles are governed by the applicable Creative Commons License

oxidation states with CSP applications was targeted on hydrogen production via water splitting (WS).[1] It attracted renewed attention due to its direct adaptability to carbon dioxide splitting (CDS) and consequent syngas production according to the scheme of reactions (1), (2) where oxidation of the reduced state of the oxide by steam or/and carbon dioxide follows a common endothermic thermal-only reduction step of the oxidized oxide state.[2] The necessary "renewable" heat for this endothermic step (and also for performing the exothermic step producing hydrogen/syngas at an adequately high temperature for kinetic reasons) can come from concentrated solar energy. Furthermore, additional relevant applications have emerged recently. Indicatively, oxidation of the reduced phase of the oxide with air (reaction (3)) can be used for thermochemical storage (TCS) of solar heat[3] and recovery of the thermal energy utilized in reaction (1) off-sun and at will or/and air separation[4]

$$MeO_x + \Delta H \leftrightarrow MeO_{x-\delta} + \delta/2O_2 \quad (1)$$

$$MeO_{x-\delta} + \delta H_2O(\delta/2\ CO_2) \leftrightarrow MeO_x + H_2\,(CO) + \Delta H \quad (2)$$

$$MeO_{x-\delta} + \delta/2O_2 \leftrightarrow MeO_x + \Delta H \quad (3)$$

The two steps of these cycles are favored at different temperature levels; thermal reduction requires higher temperatures than oxidation. Hence their cyclic implementation takes place in a so-called temperature-swing operation. This mode can be substituted or complemented by pressure-swing operation, i.e., by performing the two steps at different oxygen partial pressures (and at the same or different temperature levels—isothermal/nonisothermal cycles, respectively) to influence the driving force and equilibrium state of the reactions. Therefore, irrespective of the redox oxide chemistry's targeted thermochemical cyclic application, the efficient implementation of the proposed concepts in practice requires an appropriate redox material, a suitable reactor design, and an optimized cyclic operation strategy.[5]

2. Choice of Redox Material Composition

Although there exist commonalities in the type of redox oxide thermodynamics and material properties that are beneficial and in the operation boundary conditions, it should be borne in mind that the best material choice can be—and usually is—different in each application case. In a recent publication of the authors' group[6] the redox thermodynamics of the various state-of-the-art oxide material families were analyzed to provide insight into the theoretical limitations imposed on such processes and to guide the selection of the most suitable materials and conditions per specific application. Concerning TCS applications, for stoichiometric, single- or multimetal–cation redox pair (oxidized/reduced state) oxide systems like Co_3O_4/CoO, Cu_2O/CuO, BaO_2/BaO, Mn_2O_3/Mn_3O_4 [7] or $(Mn,Fe)_2O_3/(Mn,Fe)_3O_4$[8] reactions (1) and (3) take place at a specific, unique equilibrium temperature (T_{eq})[3] characterized by specific weight change (due to oxygen loss/gain) according to the oxides' pair stoichiometry as written above and specific enthalpy values. In contrast, nonstoichiometric (or otherwise called partial reduction) redox materials are characterized by a continuous, quasi-linear partial reduction over a wide temperature range.[9] This attribute of continuous O_2 uptake/ release can be beneficial in coupling thermochemical to sensible storage within a wide temperature range. Furthermore, the reaction extent δ and the consequent weight and enthalpy changes, depend also on the particular temperature and partial pressure of oxygen reached during the process, in addition to the kind of the material.

The three state-of-the-art relevant material families for partial (nonstoichiometric) redox reactions, ceria ($CeO_{2-\delta}$),[5] ferrites ($MFe_2O_{4-\delta}$, M = Ni, Co, Mn, Cu, Zn, Mg, etc.)[10] and perovskites $ABO_{3-\delta}$ (A = Mg, Sr, Ca, etc. and B = Fe, Mn, Co, etc.)[11] operate in a similar manner and suffer from the same limitations imposed basically by the small width of change in the non-stoichiometry δ. Ferrites- and ceria-based redox pairs are mainly utilized in WS or CDS processes and have been demonstrated on pilot scale solar reactors; between them only ceria has shown so far excellent stability of both structure and fuel productivity in long-term tests of hundreds of cycles.[12]

Perovskites offer great versatility, due to the large number of cation combinations and their tunable thermodynamic characteristics, making them well suitable for WS and CDS as well as thermochemical storage (TCS) and air separation applications, depending on their composition.[13] Pure and doped Ca–Mn-based compositions provide high enthalpies of reduction accompanied by significant δvalues at temperatures below 1000 °C,[9,14] attributes that render them attractive for TCS[15] and air separation.[16] Furthermore, such perovskite compositions are compatible with the current trends for using low cost and environmentally-benign and non-toxic materials in energy-related applications.

3. Implementation and Reactor Concepts

Despite a wealth of lab-scale studies devoted on optimizing TCS-targeted perovskite material compositions with respect to reaction enthalpy and thermal stability based on reduction/oxidation thermodynamics and reactions kinetics that has recently emerged,[17] most of such studies are limited to thermogravimetric analysis (TGA)-relevant small scale powdered or pelleted samples. Redox-oxide-based TCS is still in its infancy concerning large-scale system deployment, compared to sensible-only thermal energy storage (TES) concepts implemented on inexpensive solids or molten salts.

Redox oxide-based thermochemical reactor/heat exchanger TCS design concepts, amenable for eventual implementation in commercial, utility-scale CSP plants, emanate from approaches of sensible-only high-temperature storage in ceramic media already industrially practiced (especially in high-temperature, energy-intensive industries) or currently under consideration and investigation. These concepts can be categorized in two broad groups depending on whether the solid oxide is also employed as the solar energy harvesting medium and consequently as the heat transfer fluid (HTF) or not.

Using particle streams as a combined HTF and TCS storage medium originates from ideas considering inexpensive, chemically inert, refractory ceramic particles as alternative heat transfer and extremely high-temperature sensible heat storage ($T > 1000$ °C) media for CSP plants.[18] Redox oxide particle streams in their oxidized state are construed to be transported to the top of a solar tower where they are thermally reduced in a solar particle receiver like, e.g., a rotary kiln[19] or a packed, fluidized or

© 2022 The Authors. Advanced Energy Materials published by Wiley-VCH GmbH

16146840, 2022, 10, Downloaded from https://onlinelibrary.wiley.com/doi/10.1002/aenm.202102882 by Dtsch Zentrum F. Luft-U. Raum Fahrt In D. Helmholtz Gemein., Wiley Online Library on [05/12/2022]. See the Terms and Conditions (https://onlinelibrary.wiley.com/terms-and-conditions) on Wiley Online Library for rules of use; OA articles are governed by the applicable Creative Commons License

16146840, 2022, 10, Downloaded from https://onlinelibrary.wiley.com/doi/10.1002/aenm.202102882 by Dtsch Zentrum F. Luft-U. Raum Fahrt in D. Helmholtz Gemein., Wiley Online Library on [05/12/2022]. See the Terms and Conditions (https://onlinelibrary.wiley.com/terms-and-conditions) on Wiley Online Library for rules of use; OA articles are governed by the applicable Creative Commons License

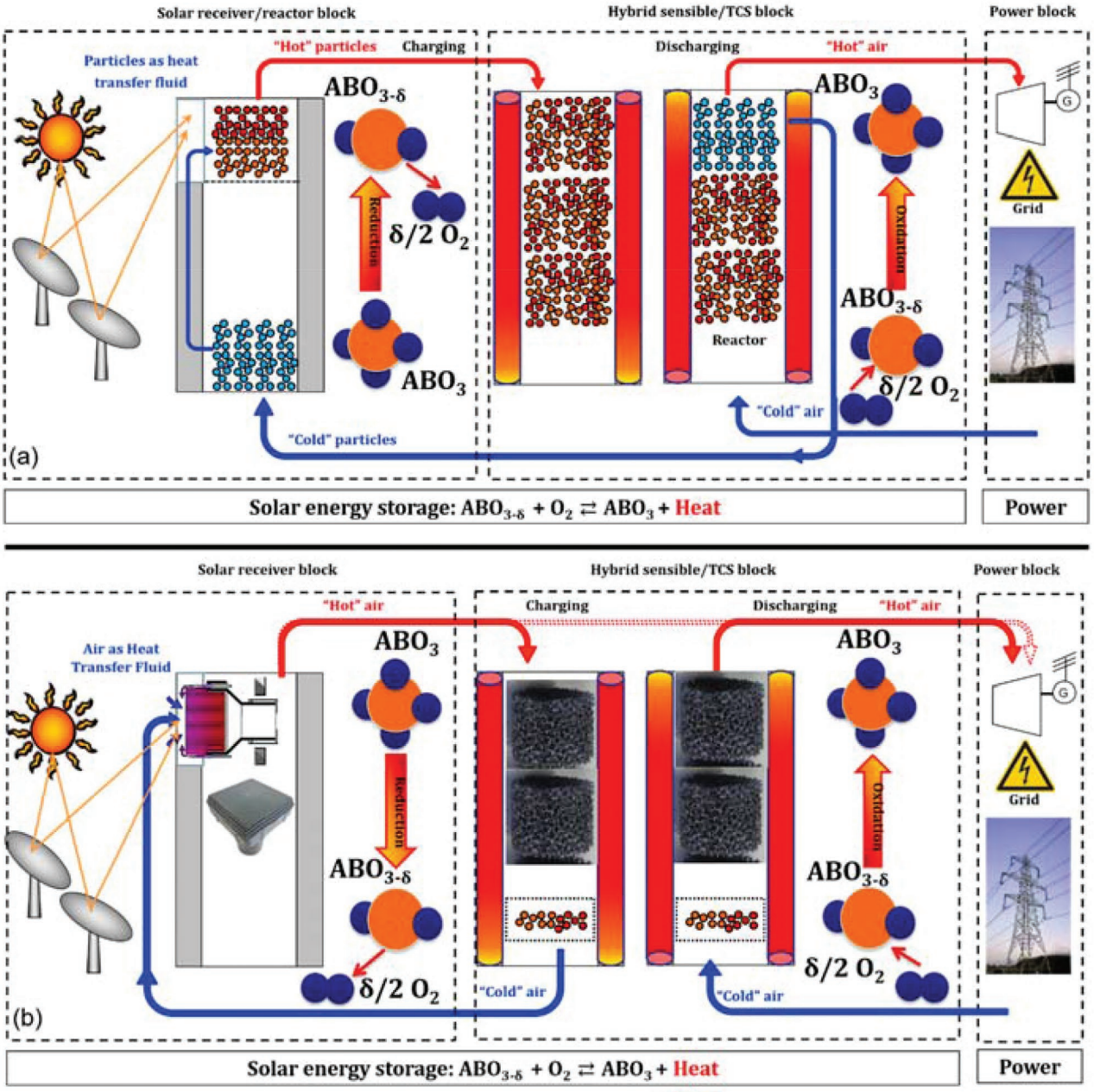

Figure 1. Conceptual scheme of thermochemical storage in CSP plants, implemented with: a) moving redox oxide particle streams employed as the heat transfer fluid; b) nonmoving redox oxide porous structures (or particle beds), spatially decoupled from a solar receiver and air as the heat transfer fluid. ABO_3 perovskites are shown as exemplary redox oxide.

spouted bed,[20] as schematically illustrated in **Figure 1**a. Their reduction is usually facilitated by application of slight vacuum ($P_{O2} \geq 100$ Pa). The reduced particles are stored in a hot storage tank and fed on-demand to an oxidation reactor where they are contacted with compressed air for heat generation. In the first relevant modeling studies, cobalt[21] and iron[22] oxides were employed; the concept was patented later utilizing mixed ionic-electronic conductive (MIEC) perovskite particles.[15d] The design, and construction, and testing under simulated solar irradiation from a high flux solar simulator (HFSS) at Georgia Institute of Technology's (GTech) facilities, of a 5 kW_{th}-scale solar thermochemical reactor operating under vacuum was reported, targeted to the first stage of the process, the solar-driven thermal reduction of a continuous, gravity-driven flow of aluminum-doped calcium manganite particles.[23] A scaled-up 100 kW_{th} version of this reactor was subsequently built by the GTech group and is planned to be tested in on-sun operation. In parallel, a vertical gravity-driven particles flow concept was also selected for the second step of the process namely (pressurized) oxidation, and a relevant smaller, bench-scale 1 kW vertical tubular reactor has been manufactured, heated so far by an electrical resistive furnace and not yet under solar irradiation.[24]

Alternatively, the oxide may not be used as a circulating HTF, but can be stationary, spatially decoupled from the solar receiver

© 2022 The Authors. Advanced Energy Materials published by Wiley-VCH GmbH

16146840, 2022, 10, Downloaded from https://onlinelibrary.wiley.com/doi/10.1002/aenm.202102882 by Dtsch Zentrum F. Luft-U. Raum Fahrt In D. Helmholtz Gemein., Wiley Online Library on [05/12/2022]. See the Terms and Conditions (https://onlinelibrary.wiley.com/terms-and-conditions) on Wiley Online Library for rules of use; OA articles are governed by the applicable Creative Commons License

and indirectly heated via another HTF as schematically illustrated in Figure 1b. Air is the obvious HTF choice in the case of oxide TCS systems. Hot air from the receiver during on-sun operation can be pumped through the volume of a nonmoving oxide storage medium in the form of a bed of particles or of porous, monolithic, flow-through structures like honeycombs, bricks, or foams, heating it sensibly ("charging") and simultaneously reducing it, coming in direct contact with it. During off-sun operation "cold" air is introduced and flows through the volume of the hot solid storage medium; therein air is not only sensibly heated while the solid medium is cooled ("discharging") but also oxidizes the solid and consequently is additionally heated by the exothermic oxidation reaction's enthalpy to the levels required for its introduction to the power block. Again, this approach originates from commercial high-temperature ceramic regenerative storage systems, e.g., the so-called Cowper stoves[25] as well as similar sensible heat storage units employed in air-operated solar thermal power plants, like the one of DLR (German Aerospace Center) at Juelich, Germany.[26]

This latter approach has been set forth by an international consortium including the authors' group, evolving from small- to larger-scale porous redox structures.[27] It has culminated in a 74 kWh_{th} pilot-scale TCS unit of 90 kg of Co_3O_4 coated on cordierite honeycombs, which clearly showed reversible temperature effects on an air stream due to chemical reactions during both charging and discharging,[28] and represents one of, if not the largest oxide-based TCS system developed and experimentally validated so far. Very recently, the same isothermal charging and discharging was reported by another group on honeycombs made entirely of $(Mn_{0.8}Fe_{0.2})_2O_3$, of a total mass of 110 g.[29] Some variations even involve separation of the sensible and TCS systems and use of an additional heat exchanger.[17d,18a,30]

Both approaches essentially thrive to increase the volumetric and/or gravimetric energy storage capacity, exploiting the redox reactions' enthalpy upon thermal cycling of the storage material. Hence, they have the potential of greatly shrinking the size of storage subsystems/tanks.

Naturally, each approach has advantages and drawbacks. TCS based on nonmoving structured porous ceramics only circulates gas streams, thereby avoiding circulation of hot solid particles and associated sintering, attrition, erosion, wear, sealing and fine particles elutriation and separation issues as well as movement of mechanical parts at high temperatures. Technically, this approach can be also implemented with nonmoving packed beds of particles, shaped in the form of granules[31] (indicated with the dotted box at the bottom part of Figure 1b). In fact, along the same rationale of employing earth-abundant, environmental-friendly and inexpensive redox materials, TCS operation of such beds made of $(Mn,Fe)_2O_3/(Mn,Fe)_3O_4$ redox granules,[32] and of Cu_2O/CuO ones[33] and scales of ≈500 g and ≈100 g, was indeed demonstrated by research groups of DLR (German Aerospace Center) and ETH (Swiss Federal Institute of Technology in Zurich) respectively.

4. Structured Porous Ceramics in TCS

Critical to the implementation of large-scale monolithic porous ceramics in TCS is the reversible cyclability with respect to thermodynamic characteristics, thermal stress resistance, macroscopic structural integrity, and durability. Irreversible expansion upon thermal cycling, as seen in many redox oxide-based systems considered not only for TCS[34] but for WS/CDS as well[35]—leading to extensive microcracking observed in our previous work on cobalt oxide and iron oxide foams[27b,36]—has to be avoided. The effect could be mitigated by coating the redox oxide on cordierite supports,[37] but at the cost of reduced active material load and hence reduced storage capacity. This approach has been subsequently adopted from other research groups exploring TCS through the calcium oxide hydration/dehydration scheme by coating silicon carbide foams with calcium hydroxide.[38] Furthermore, perovskite-coated reticulated porous ceramics (RPCs, also known as "ceramic foams"[39]) are also explored in the context of CDS.[40]

Recent works of the authors' group have identified $CaMnO_{3-\delta}$ as one of the most promising out of twelve Ca–Mn- and Sr–Fe-based compositions investigated with respect to their oxygen release/uptake and corresponding heat effects.[16,41] To take the next step toward the envisaged larger-scale testing of monolithic foam structures in TCS concepts, we demonstrate the manufacturing of stable, sturdy foams made entirely out of $CaMnO_3$ in cylindrical shapes up to 2 cm in diameter and length in the present work.

It has to be mentioned that shaping of similar perovskite compositions has been reported in the literature; structured small-size $Ca_{0.9}Mn_{0.5}Ti_{0.5}O_{3-\delta}$ pellet extrudates have been manufactured and tested as oxygen carrier materials for fixed-bed chemical looping combustion for syngas production.[42] $Ca_{0.95}Sm_{0.05}MnO_3$ porous foams have been manufactured and tested as thermoelectric generator (TEG) modules up to 575 °C.[43] However, applications relevant to thermochemical storage performed with structured ceramic redox all-perovskite foams are, to the best of our knowledge, reported here for the first time. The accompanying evaluation of critical characteristics, such as thermal expansion and contraction, mechanical strength, thermogravimetric and calorimetric values in the light of long-term multicycle applications, provides an extensive basis to proceed to large-scale demonstration of monolithic, porous perovskite structures in relevant thermochemical processes.

5. Results and Discussion

In contrast to most reported RPC recipes, sturdy and rigid foams could be produced without the addition of binder. While a detailed study on influencing factors of the manufacturing process is currently ongoing, the present work focuses on the key parameters of the final product in comparison to other relevant redox specimens. Hence, all results on perovskite foams shown are retrieved from 30 ppi (pores per linear inch) foams, prepared with an 80%wt solid content and 3%wt dispersing agent as described in Section 7. Samples of various sizes are shown in **Figure 2**.

5.1. Porosity and Pore Size Distribution

The porosimetry results are summarized in **Figure 3** in plots with a common *x*-axis scale. Figure 3a,b shows the cumulative curves of pore volume per g of material of a typical as-prepared foam, to indicate the relevant contribution of macro- and

© 2022 The Authors. Advanced Energy Materials published by Wiley-VCH GmbH

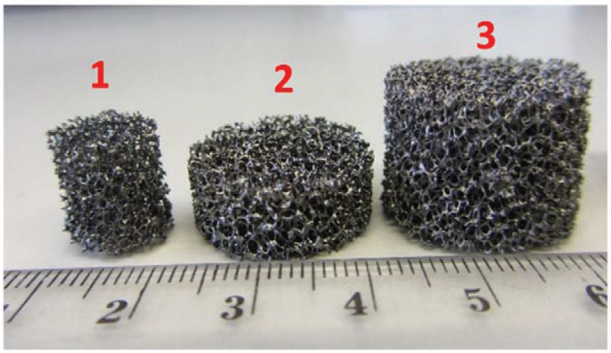

Figure 2. Prepared $CaMnO_3$-foams of various dimensions, made from 30 ppi PU-templates. 1) ⌀1 × 1,2 cm used for TGA; 2) ⌀2 × 1 cm used for mechanical strength tests; 3) ⌀2 × 2 cm.

meso/micropores, respectively, to the total (struts) porosity. Pores with a diameter below 300 nm make up ≈10% of the total pore volume. The Hg and N_2 differential pore volume distribution curves in Figure 3a,b indicates the relevant macro-and meso/micropore diameters at ≈38 µm and ≈4 nm respectively.

The differential and normalized cumulative (in cc/cc, from where the porosity can be calculated) Hg porosimetry curves of two representative $CaMnO_3$ structures, a foam and a sintered bar employed for TGA and dilatometry tests respectively, are compared in Figure 3c. As expected, the foam exhibits a higher total macro-porosity of 16.2% compared to 10.8% of the bar, since the latter has been sintered for almost seven times longer.

Figure 3d shows the Hg porosimetry curves of the specimens of the three compounds, $CaMnO_3$, Co_3O_4, and mixed Fe–Mn oxide, out of which bars used in the dilatometry experiments were sectioned (Figure S3 and Table S1, Supporting Information). The results reflect the impact of sintering temperature and long dwelling times on porosity. The mixed Mn–Fe oxide, sintered at a much higher temperature than the respective Co_3O_4 pellet, exhibits pores in the range 10–100 µm without a distinct mean peak. In contrast, the Co_3O_4 and $CaMnO_3$ samples exhibit a narrow pore size distribution around a mean diameter of 5 µm, with the former demonstrating ≈ 5 times higher pore volume fraction originating from the much lower sintering temperature and time.

5.2. Mechanical Strength

The evolution of applied pressure versus time for two $CaMnO_3$ foam specimens is shown in **Figure 4** (top). As seen therein the perovskite foams do not exhibit a distinct point of failure when placed under pressure load. Instead, the weakest struts start to break one after the other until eventually the whole foam collapses.

The failure pressures of the specimens have been determined by the first fracture of the foam, leading to withstanding pressure loads of 132.4 and 87.5 kPa respectively for the two specimens. Photographs of the specimens during fracture (Figure 4, bottom) indicate that fracture predominantly appears in the outer region of the foam and at an angle with respect to the direction of pressure load. The applied pressure loads compare to approximately 1.324 and 0.875 bar, showing that pressurized airflow through the structure (e.g., charging/discharging of a thermal storage process) is possible.

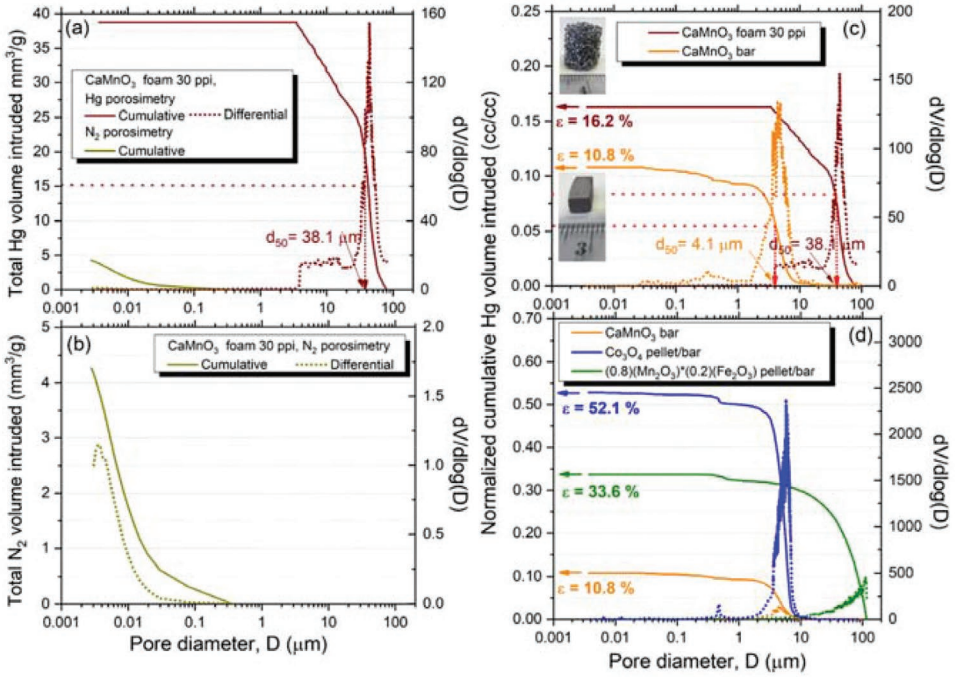

Figure 3. Porosimetry characterizations: a,b) $CaMnO_3$ foam, N_2 and Hg pore volume distribution curves, respectively; c,d) differential and normalized cumulative Hg porosimetry curves from where median macro-pore diameter and porosity can be determined as shown for c) $CaMnO_3$ foam and bar used for dilatometry experiments; d) all specimens out of which bars used for the dilatometry experiments were sectioned.

© 2022 The Authors. Advanced Energy Materials published by Wiley-VCH GmbH

16146840, 2022, 10, Downloaded from https://onlinelibrary.wiley.com/doi/10.1002/aenm.202102882 by Dtsch Zentrum F. Luft-U. Raum Fahrt In D. Helmholtz Gemein., Wiley Online Library on [05/12/2022]. See the Terms and Conditions (https://onlinelibrary.wiley.com/terms-and-conditions) on Wiley Online Library for rules of use; OA articles are governed by the applicable Creative Commons License

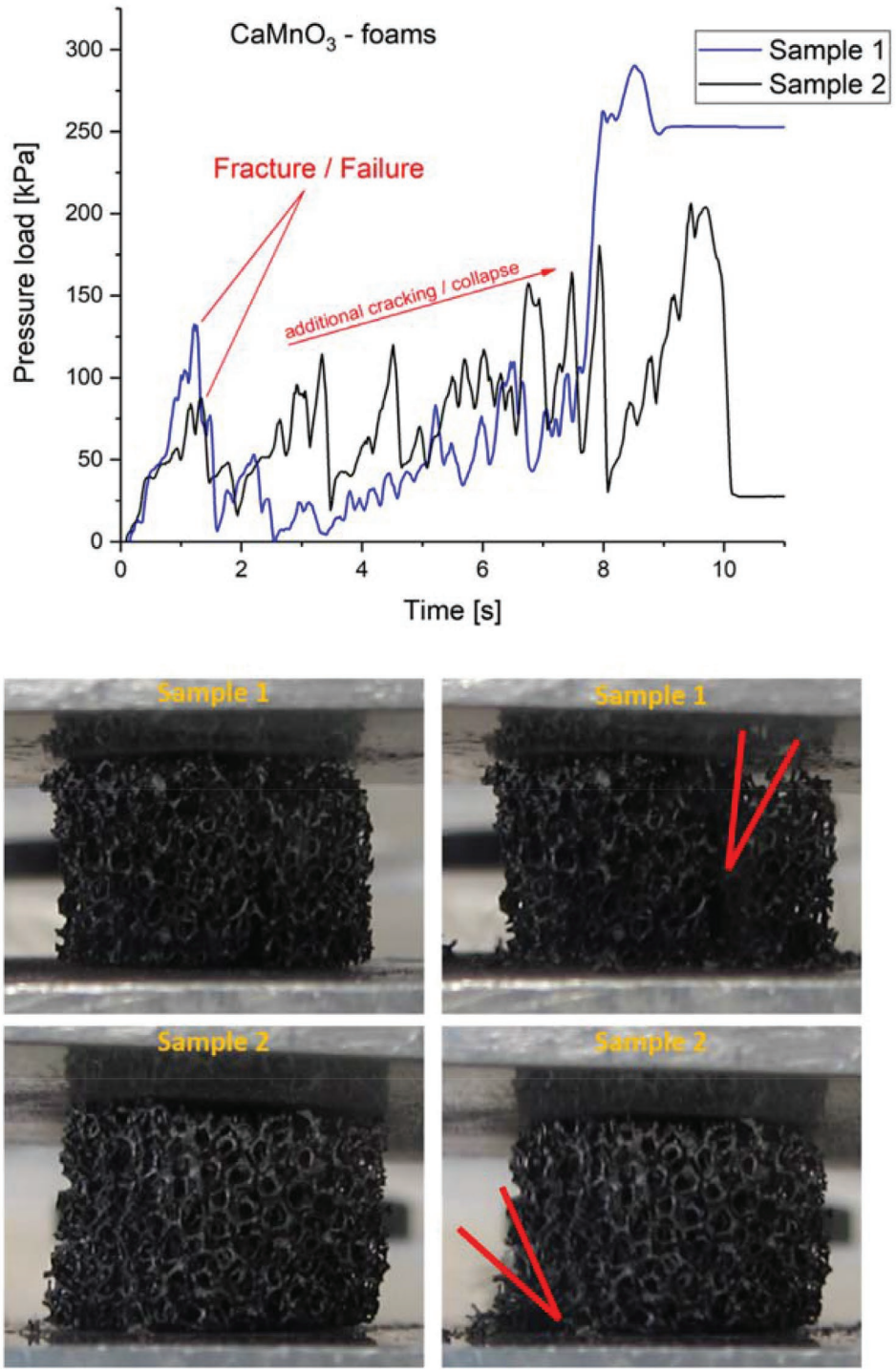

Figure 4. $CaMnO_3$-foams under pressure load. Top: Pressure load over time, first peak pressure indicates initial fracture/failure. Bottom: Corresponding foam samples during the measurement; left: pristine samples at the start, right: foam samples at time of failure as indicated in top graph, point of fracture outlined in red.

5.3. Thermal Redox Cycling

A powder sample of $CaMnO_3$ and two identical foams made from this powder were cycled in a TGA under synthetic air in the range of 300–1100 °C. It can be seen (**Figure 5**) that both foams exhibit practically identical behavior, very similar to that of the powder, demonstrating completely reversible and reproducible weight loss/gain from cycle to cycle. The weight loss during heating is fully reversible upon cooling. No significant shift of the values can be observed over the first five cycles for all three samples.

© 2022 The Authors. Advanced Energy Materials published by Wiley-VCH GmbH

16146840, 2022, 10, Downloaded from https://onlinelibrary.wiley.com/doi/10.1002/aenm.202102882 by Dtsch Zentrum F. Luft-U. Raum Fahrt in D. Helmholtz Gemein., Wiley Online Library on [05/12/2022]. See the Terms and Conditions (https://onlinelibrary.wiley.com/terms-and-conditions) on Wiley Online Library for rules of use; OA articles are governed by the applicable Creative Commons License

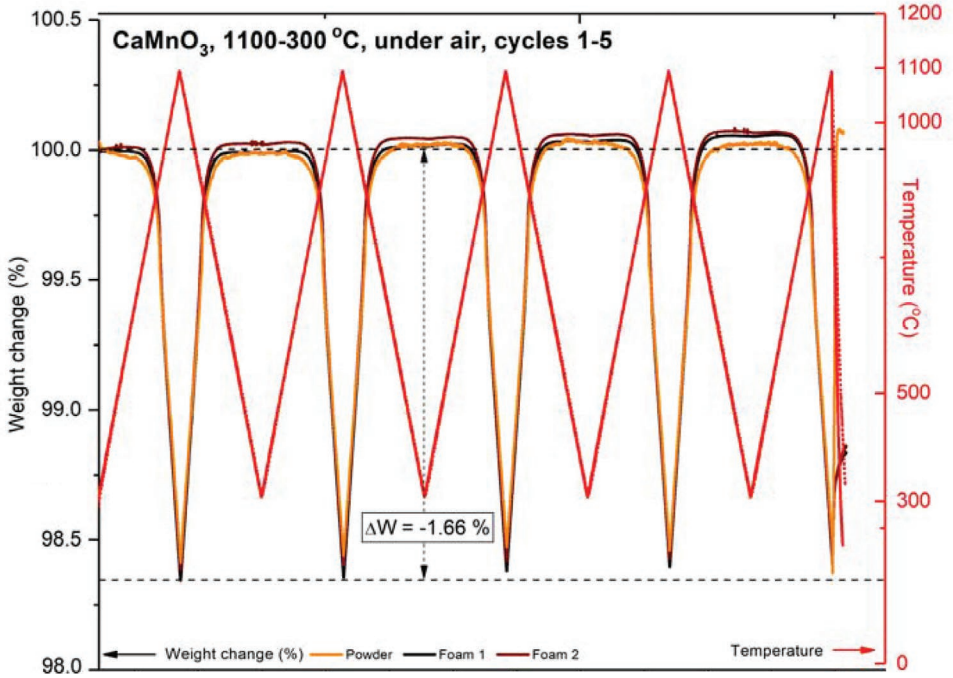

Figure 5. TGA comparison of two $CaMnO_3$ foams versus the respective powder: 5 cycles between 1100 and 300 °C, last cooling step under argon.

Foam No. 1 was fractured to be characterized with respect to phase composition and microstructure. The XRD spectrum of (crushed powder from) this foam after the five TGA cycles is compared to those of the starting $CaMnO_3$ powder and of the foams before TGA (obtained with powder from the foam fragments after the crushing strength tests) in **Figure 6**. It can be seen that a small, yet distinguishable amount of the marokite phase, $CaMn_2O_4$, has been formed during the reduction stage(s) of the redox cycling —clearly absent in both the "starting" powder and foams. $CaMnO_3$ is known to disproportionate into marokite and spinel compositions at high temperatures and low pO_2. These conditions were repeatedly applied, especially in the last cycle of each TGA run, and are the reason for the detected marokite side phase.

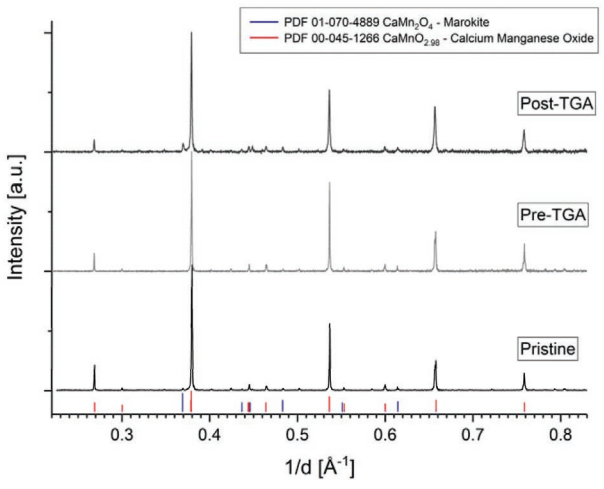

Figure 6. Phase composition (XRD spectra) comparison among the $CaMnO_3$ powder and the respective foam No 1 before (pre-TGA) and after (post-TGA) cyclic TGA experiments, where the formation of a minor second marokite phase can be distinguished after redox cycling.

Foam No 2 was further tested for 41 more cycles totaling 46 cycles, in segments of 5 and 12 cycles. The results are shown in **Figure 7**. Cycles 35–46 exhibit a drift that is attributed to changes in the atmospheric pressure around the measurement system, but do not weaken the meaningfulness of the %wt-loss/gain of each individual cycle. Maximum %wt-changes, together with the applied oxygen concentration, for each individual cycle are depicted in **Figure 8**. It can clearly be seen that the foam exhibits a nearly constant total weight loss/gain of around 1.66%wt practically identical in every cycle during all 5-cycle and 12-cycles sets, with specific increases/decreases depending on the applied oxygen concentration.

Cycles 11 and 22 are marked identical to Figure 7. While in cycle 11 the sample was only heated up to 1000 °C and therefore shows a significantly lower maximum %wt-loss compared to the other cycles, cycle 22 was carried out under pure argon, and therefore with significantly reduced oxygen partial pressure, resulting in a higher maximum %wt-loss. The influence of temperature and oxygen partial pressure on the weight loss becomes evident in Equation 1. Both, higher temperatures and lower oxygen partial pressures shift the reaction toward the reduced state (right side of reaction in Equation 1), resulting in greater weight loss. In contrast, lower temperatures and higher oxygen partial pressures shift the reaction toward the oxidized state (left side of Equation 1) and result in smaller weight loss. Comparing cycles 11, 22 as well as the cycles 18–21 (carried out under increased $p(O_2)$ with the remaining cycles it can be concluded that a temperature difference of 100 °C in cycle 11 has a much stronger influence on the maximum %wt-loss, and respectively on the reduction extent of the $CaMnO_3$ foam

© 2022 The Authors. Advanced Energy Materials published by Wiley-VCH GmbH

16146840, 2022, 10, Downloaded from https://onlinelibrary.wiley.com/doi/10.1002/aenm.202102882 by Dtsch Zentrum F. Luft-U. Raum Fahrt In D. Helmholtz Gemein., Wiley Online Library on [05/12/2022]. See the Terms and Conditions (https://onlinelibrary.wiley.com/terms-and-conditions) on Wiley Online Library for rules of use; OA articles are governed by the applicable Creative Commons License

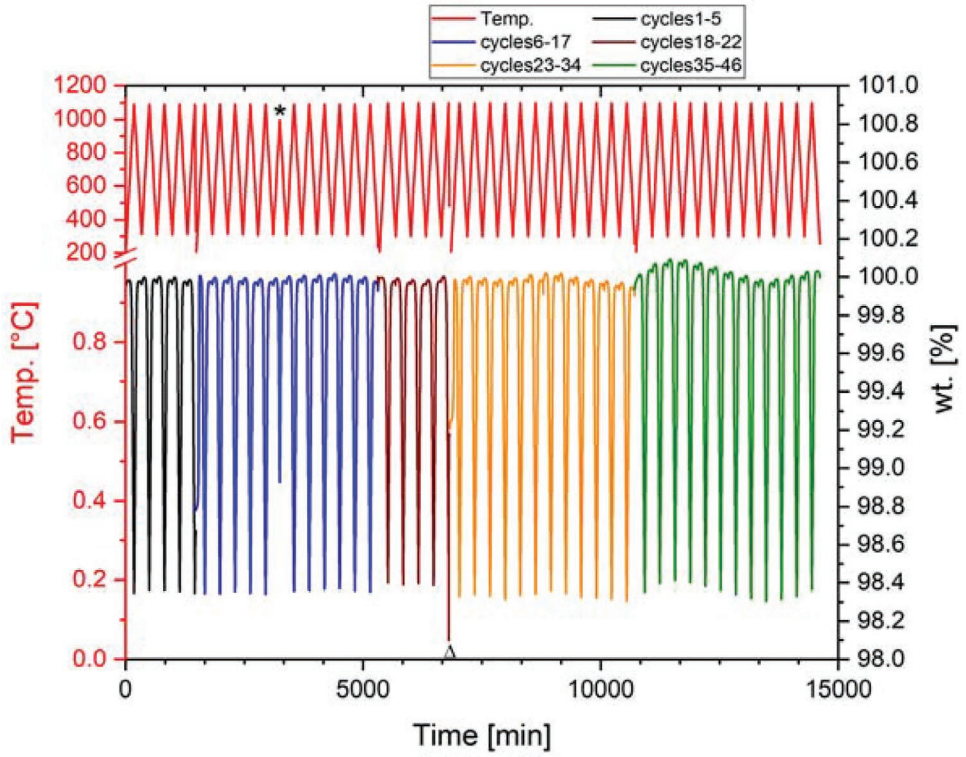

Figure 7. $CaMnO_3$ foam No. 2 cycled 46 times up to 1100 °C. Cycles 11 and 22 (marked with * and Δ) are only reduced up to 1000 °C (*) or under pure argon (Δ).

samples, than the reduced $p(O_2)$ in cycle 22 or the increased $p(O_2)$ in cycles 18–21. Reduction and oxidation are fully reversible over the range of 46 cycles, showing exceptional redox stability.

As shown in **Figure 9**, foam 1 after 5 cycles and foam 2 after 46 cycles do not exhibit any visible deformation compared to the as-prepared samples. This attribute is crucial for the implementation of such foams into reactor systems where macroscopic as well as thermomechanical stability is needed.

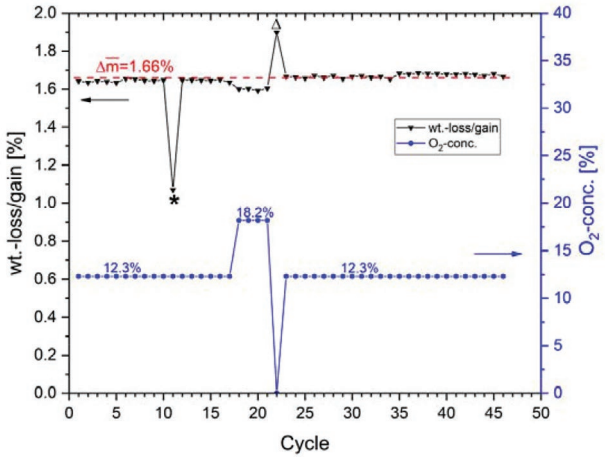

Figure 8. Results of maximum %wt loss/gain and the applied O_2-concentration over 46 cycles of $CaMnO_3$ foam. The cycles 11 (*) and 22 (Δ) are marked as in Figure 7.

5.4. Microstructure

Characteristic SEM photographs of an as-manufactured $CaMnO_3$ foam, of the foam after five TGA cycles and of an as-sintered $CaMnO_3$ bar not subjected to dilatometry, are shown in **Figure 10**. After their sintering, the foams are characterized by a "dense"-struts structure (Figure 10a) with intra-particle and grain boundaries porosity (Figure 10b). As can be seen in Figure 10c, the struts have a "hollow triangular" structure, typical for ceramic foams manufactured via the polyurethane (PU) replica route.[39,44] The "dense walls" microstructure (Figure 10b) is maintained after the five TGA cycles (Figure 10d). The microstructure is very similar to that of the sintered bar (Figure 10e,f), showing similar intra-particle and grain boundary pores. Characteristic EDS elemental microanalysis spectra showing qualitatively the sintered objects' elemental composition are shown in Figure S4 (Supporting Information).

5.5. Thermal Expansion and Phase Transition

The results of the dilatometry experiments for the three specimens tested, $CaMnO_3$ and the two referential Co_3O_4 and $(Mn,Fe)_2O_3$ compositions, are shown in **Figure 11** in the form of relative length change ($\Delta L/L_o$) and coefficient of thermal expansion (CTE) over the five heating and cooling cycles. The CTE is calculated as $(L - L_o)/(T - T_o)$ with L_o being the initial length of the specimen at ambient temperature T_o.

© 2022 The Authors. Advanced Energy Materials published by Wiley-VCH GmbH

16146840, 2022, 10, Downloaded from https://onlinelibrary.wiley.com/doi/10.1002/aenm.202102882 by Dtsch Zentrum F. Luft-U. Raum Fahrt In D. Helmholtz Gemein., Wiley Online Library on [05/12/2022]. See the Terms and Conditions (https://onlinelibrary.wiley.com/terms-and-conditions) on Wiley Online Library for rules of use; OA articles are governed by the applicable Creative Commons License

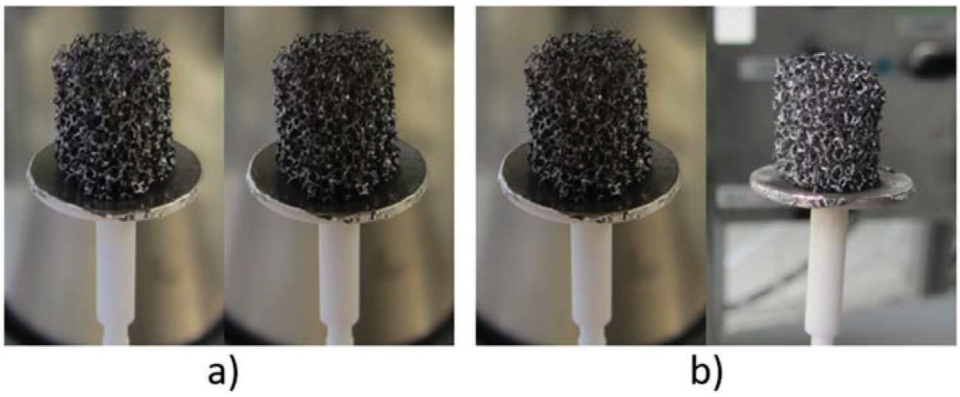

Figure 9. a) Foam 1 before (left) and after (right) 5 cycles 300–1100 °C. b) Foam 2 before (left) and after (right) 46 cycles 300–1100 °C. Both foams were manufactured identically.

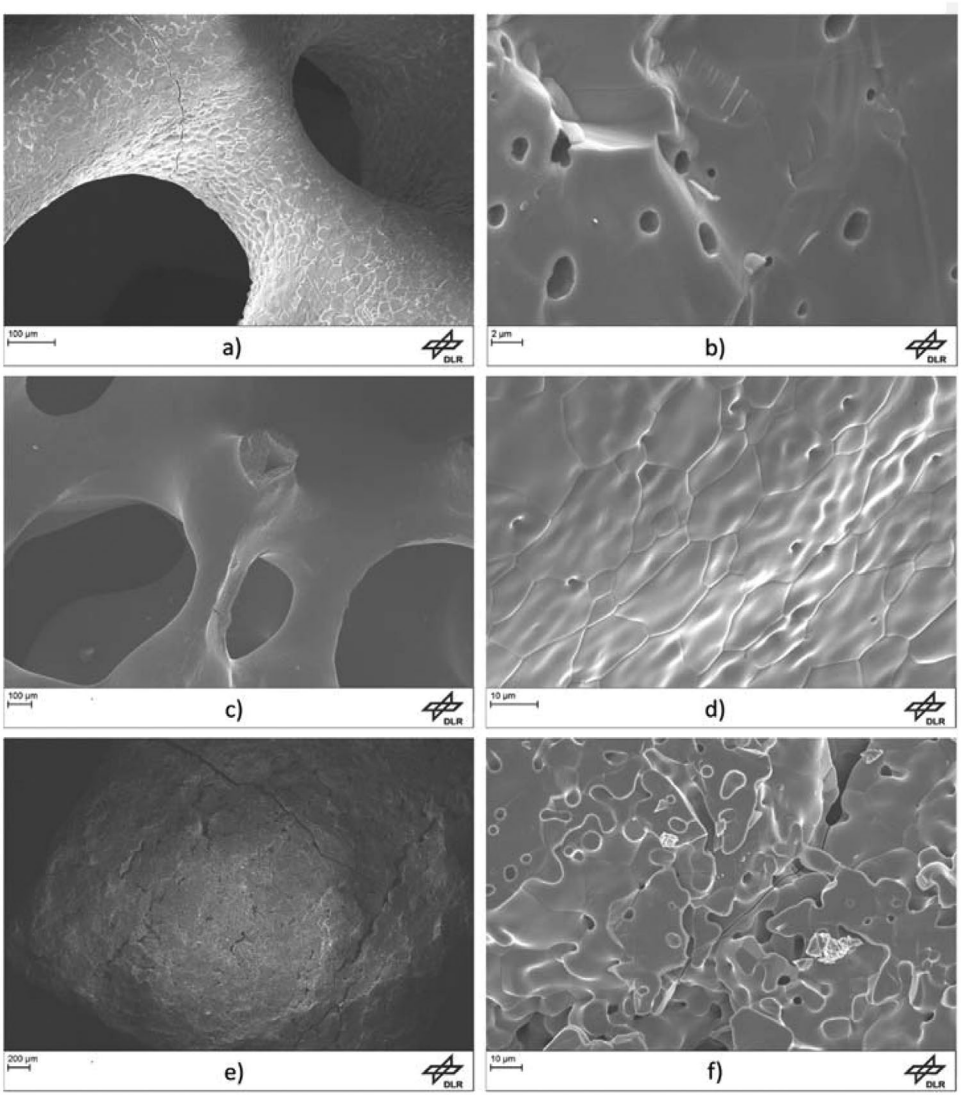

Figure 10. SEM photographs of a,b) as-prepared $CaMnO_3$-foam, c,d) $CaMnO_3$-foam after 5 TGA cycles, e,f) as-prepared $CaMnO_3$-bar.

© 2022 The Authors. Advanced Energy Materials published by Wiley-VCH GmbH

16146840, 2022, 10, Downloaded from https://onlinelibrary.wiley.com/doi/10.1002/aenm.202102882 by Dtsch Zentrum F. Luft-U. Raum Fahrt In D. Helmholtz Gemein., Wiley Online Library on [05/12/2022]. See the Terms and Conditions (https://onlinelibrary.wiley.com/terms-and-conditions) on Wiley Online Library for rules of use; OA articles are governed by the applicable Creative Commons License

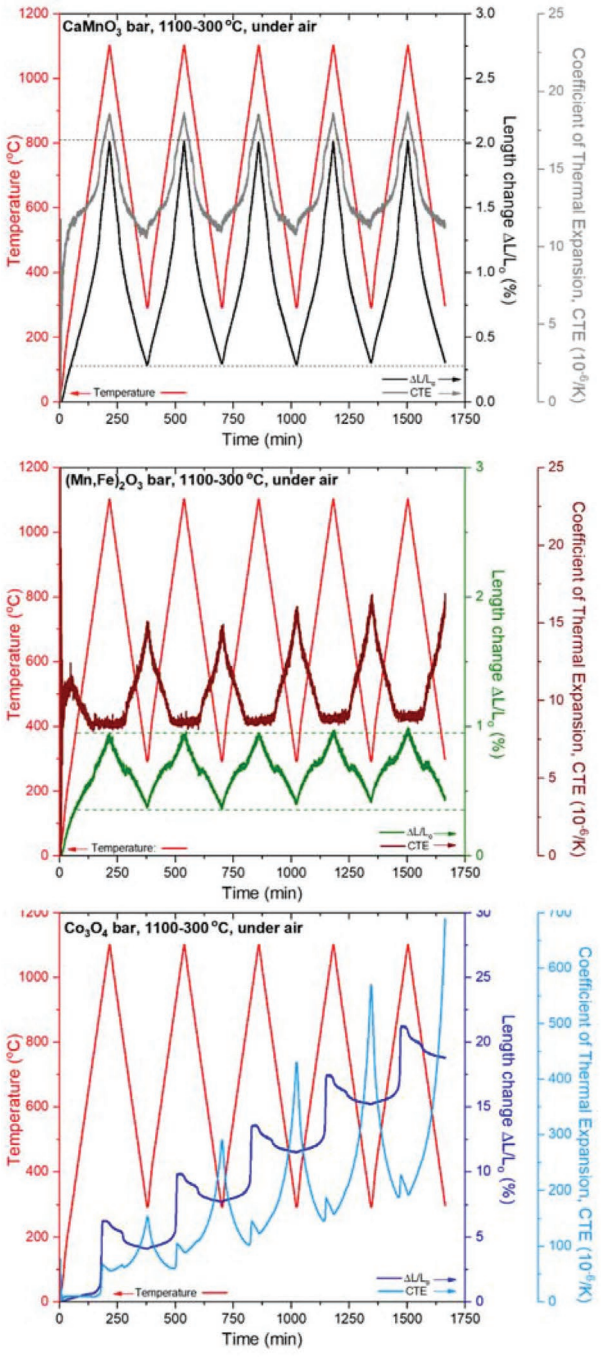

Figure 11. Thermal expansion of $CaMnO_3$ (top), $(Mn,Fe)_2O_3$ (middle), and Co_3O_4 (bottom) bar specimens. Measured by optical dilatometry in air and cycled between 300 and 1100 °C.

It is remarkable that the $CaMnO_3$ bar specimen (Figure 11, top) undergoes a completely reversible cyclic expansion/contraction from cycle to cycle. Despite a length increase of ≈2% upon heating to 1100 °C, when cooled to 300 °C, the specimen recovers exactly its original pristine dimensions. While $CaMnO_3$ and $(Mn,Fe)_2O_3$ exhibit relative length change ranges of similar magnitude ≈1–2%, Co_3O_4 spans over a much higher range up to ≈20% after the fifth cycle (Figure 11, bottom). Co_3O_4 exhibits a remarkable expansion of the order of 7% of its initial length upon each reduction step during heating. Only a minor part of this expansion is recovered as contraction in the subsequent cooling step. The major part of the expansion during reduction (heating), which is reproducible from cycle to cycle, is not recovered during oxidation (cooling) and thus the specimen exhibits a cumulative overall length increase of the order of 20% after the five-cycles test.

Given this irreversible length change in each step, the cyclic CTE curve for Co_3O_4 as calculated based on a particular ΔT and a ΔL with respect to the initial length L_o has no physical and arithmetic meaning beyond the first cycle, but is plotted on the graph just to show its scale relevant to those of the other materials. This characteristic of Co_3O_4 has been also identified on dense pellet specimens tested with an in-house heating/extensometer device in one of our previous works[27b] but not under a testing protocol comparative to other TCS-targeted redox materials.

The $\Delta L/L_o(\%)$ curve of $(Mn,Fe)_2O_3$ (Figure 11, middle) resembles to that of the $CaMnO_3$. $(Mn,Fe)_2O_3$ exhibits a relative length change similar in magnitude to $CaMnO_3$, but slightly lower, ≈1%. However, the curve is characterized by a small, but clear nonzero residual expansion after each cycle (distinguished between the horizontal dotted green lines). This is undoubtedly reflected in the slightly higher value of the CTE calculated after each cycle step ending at 300 °C (brown curve in Figure 11, middle). Even such small residual expansion within each cycle can cause severe problems if the material is cycled over a large number of cycles as it would be the case in a storage unit of a commercial-size CSP plant.

Returning to $CaMnO_3$, as already observed in our previous studies,[41] the CTE curves are characterized by a distinguishable increase of slope (inflection point), corresponding to a distinct increase of the linear expansion coefficient upon heating and a reversible decrease upon cooling. HT-XRD experiments of $CaMnO_3$ under air were performed to correlate this phenomenon to any phase transformations (**Figure 12**). The orthorhombic (*Pnma*) and the cubic ($Pm\bar{3}m$) phase share major diffraction peaks, with the latter having the higher symmetry. Diffraction peaks at ≈38.2° and ≈40.2° (2θ), that are characteristic for the orthorhombic phase, first decrease upon heating the sample and finally vanish at 900 °C, revealing the completion of an orthorhombic-to-cubic phase transition at 900 °C. The results are in accordance with previously reported temperature values for this transition.[17a,45] No tetragonal phase was identified, in contrast to previous reports.[45] The phase transition is completely reversible, shown by the recurring increase of the characteristic orthorhombic peaks upon cooling.

The interrelation of phase transformations with dimensional changes and redox reactions characteristics becomes evident by the superposition of the five-cycles TGA and dilatometer experiments (Figures 5 and 11 top) under the common time-temperature schedule as shown in **Figure 13**, where the third cycles of these experiments are compared. (The respective comparison for the other two compounds, Co_3O_4 and $(Mn,Fe)_2O_3$ are reported in Figure S5, Supporting Information). All three TGA experiments with $CaMnO_3$ samples are shown—one with powder and two with foams—together with the relevant DSC

© 2022 The Authors. Advanced Energy Materials published by Wiley-VCH GmbH

16146840, 2022, 10, Downloaded from https://onlinelibrary.wiley.com/doi/10.1002/aenm.202102882 by Dtsch Zentrum F. Luft-U. Raum Fahrt In D. Helmholtz Gemein., Wiley Online Library on [05/12/2022]. See the Terms and Conditions (https://onlinelibrary.wiley.com/terms-and-conditions) on Wiley Online Library for rules of use; OA articles are governed by the applicable Creative Commons License

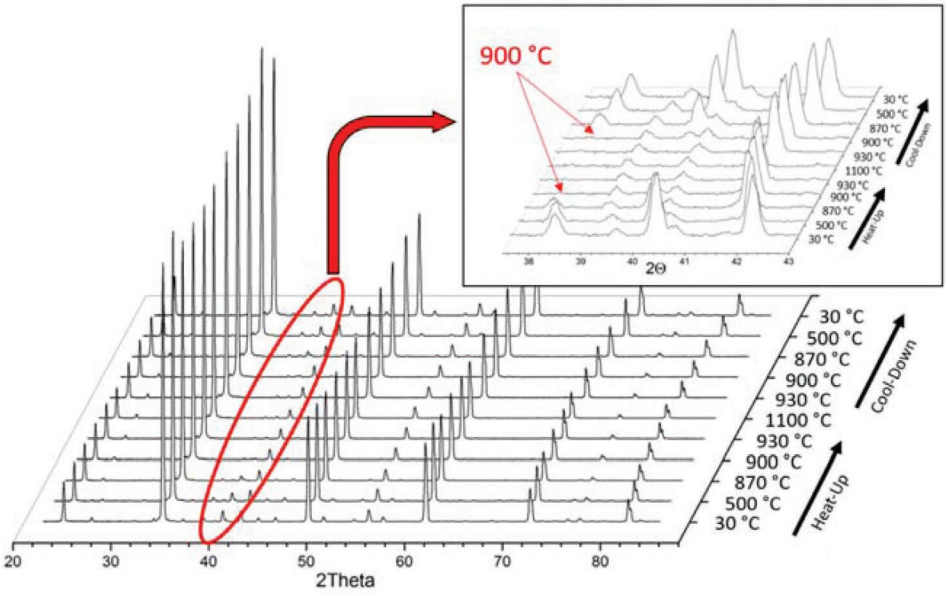

Figure 12. HT-XRD of $CaMnO_3$ conducted under air between 30 and 1100 °C. Orthorhombic peaks at ≈38.5° and ≈40.5° 2 θ; Embedded graph: magnification of relevant 2 θ range 38–43°.

curve for the powder. The observations from this graph can be outlined as follows:

- From the TGA curves, it can be clearly distinguished that the foam and powder samples exhibit similar reduction onset temperatures upon heating, beginning to significantly lose weight at around 760 °C.
- The TGA curves, in addition to their linear-w.r.t-temperature segments, also show local "sharper" inflection points indicating an "abrupt", step-type, small yet clearly distinguishable

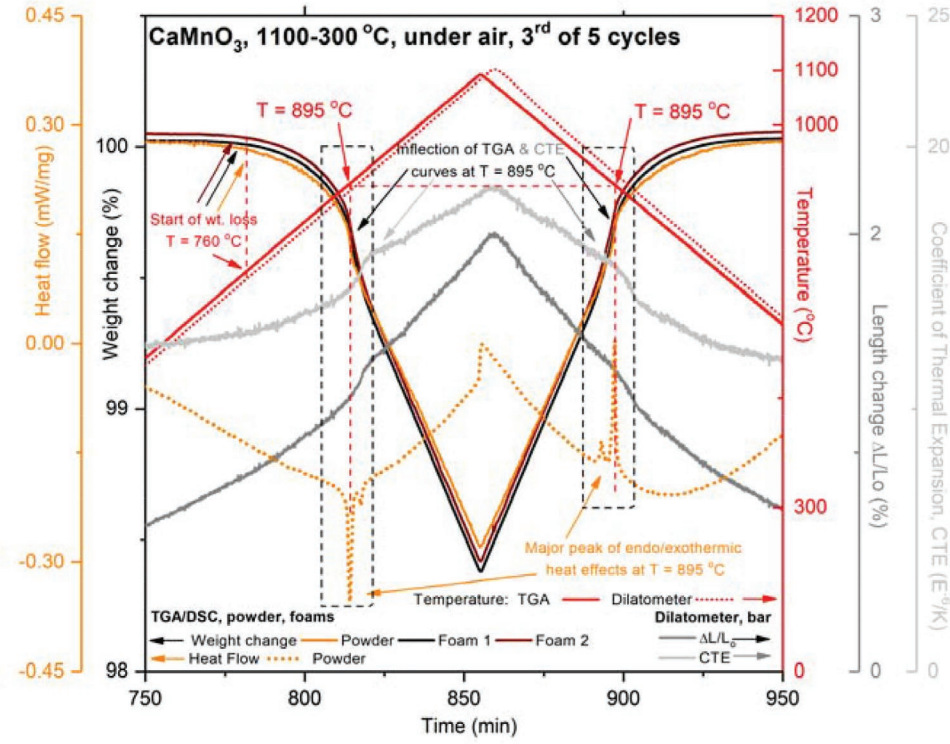

Figure 13. Superposition of weight loss/gain of $CaMnO_3$ samples (powder and foams) as obtained by TGA, DSC values from $CaMnO_3$ powder samples obtained from combined TGA/DSC measurements and length changes of the sintered $CaMnO_3$-bar samples obtained by dilatometry. Shown are extracted third cycles of each cyclic run.

© 2022 The Authors. Advanced Energy Materials published by Wiley-VCH GmbH

16146840, 2022, 10, Downloaded from https://onlinelibrary.wiley.com/doi/10.1002/aenm.202102882 by Dtsch Zentrum F. Luft-U. Raum Fahrt In D. Helmholtz Gemein., Wiley Online Library on [05/12/2022]. See the Terms and Conditions (https://onlinelibrary.wiley.com/terms-and-conditions) on Wiley Online Library for rules of use; OA articles are governed by the applicable Creative Commons License

16146840, 2022, 10, Downloaded from https://onlinelibrary.wiley.com/doi/10.1002/aenm.202102882 by Dtsch Zentrum F. Luft-U. Raum Fahrt In D. Helmholtz Gemein., Wiley Online Library on [05/12/2022]. See the Terms and Conditions (https://onlinelibrary.wiley.com/terms-and-conditions) on Wiley Online Library for rules of use; OA articles are governed by the applicable Creative Commons License

weight loss due to oxygen release, corresponding for all of them to a temperature about 895 °C (regions enclosed with a black dashed line).

- The CTE (and the $\Delta L/L_o$) curves exhibit also an inflection point at exactly the same temperature, which is in good agreement with the phase change detected in HT-XRD (900 °C, Figure 12).
- Furthermore, at exactly the same temperature range two peaks associated with reversible endothermic/exothermic heat effects are also observed on the DSC curve of the powder,[16,41] and in fact the major peak is practically collocating with respect to temperature with the inflection points of the TGA, $\Delta L/L_o$ and CTE curves (considering the minute discrepancy between the temperature profiles of the two instruments).
- These phenomena are quantitatively reproducible in all five cycles performed (not shown, but easily corroborated from Figures 5 and 11 top).

The orthorhombic structure of an ABO_3 perovskite is basically a distorted cubic one. Therefore, the structural difference between the orthorhombic and cubic phase is small. Still the high-temperature cubic phase of $CaMnO_3$ does exhibit a larger expansion coefficient than its orthorhombic counterpart. Overall, this phase change leads to a significant increase in thermal expansion, accompanied by oxygen loss and endothermal heat effects upon heating with all these phenomena being fully reversible upon cooling. While the complete reversibility of thermal expansion is a crucial parameter for the long-term stability of a storage unit, such endo- and exothermic heat effects can also contribute to the storage capacity throughout the applied temperature range.

5.6. Issues of Materials Selection and Concept Scalability

In the quest for optimal material compositions, the relevant literature has been substantially enriched with many materials-composition-screening studies, targeted on quantifying the relevant contributions of sensible and thermochemical energy stored and eventually comparing TCS to sensible-only storage in materials like inexpensive chemically inert solids and molten salts. As already elaborated in more detail in a recent publication from our group,[46] many such studies on perovskites involve thermodynamic modeling of the extent of reduction δ for a specific material composition as a function of temperature and oxygen partial pressure, complemented by TGA experiments to determine equilibrium values and produce P–T–δ relationships as charts of isothermal or isobaric or "iso-δ" curves. Parametric studies with respect to the kind and the quantity of the dopant elements, can then identify optimal material compositions and respective conditions for a given (or maximum possible) reduction extent, δ. The specific heat capacity of the various materials is calculated thermodynamically, approximated by the Dulong-Petit law, or experimentally measured under standardized DSC protocols. As a result, such properties are often provided for a wide range of specifically-doped compositions. Although already previously reported,[46] such sensible-TCS-relevant representative properties for the three systems addressed in this work are provided in **Table 1**, assembled from several such studies, in particular from.[15b,18a] With respect to the Ca–Mn-based perovskites, properties of representative doped compositions are included. It should be noted that reduction onset temperatures span a temperature range depending on the heating rate during the experiments,

Table 1. Reaction schemes, temperature ranges and thermophysical properties' comparison of redox oxide systems considered for thermochemical energy storage.

	Co oxide	Mn–Fe oxide	$CaMnO_3$ perovskites
Redox reaction scheme	$2\ Co_3O_4 + \Delta H \rightleftarrows 6CoO + O_2$	$6(Mn,Fe)_2O_3 + \Delta H \rightleftarrows 4(Mn,Fe)_3O_4 + O_2$	$CaMnO_3 + \Delta H \rightleftarrows CaMnO_{3-2x} + x\ O_2$
$T_{reductiononset}$ [°C] (at specific P_{O2})	880–925 (TGA[49]) (0.21 bar)	964-1008 (TGA[8]) (0.21 bar)	$CaMnO_3$ 760 [this study] $CaAl_{0.2}Mn_{0.8}O_3$ 750[14] $CaTi_{0.2}Mn_{0.8}O_3$ 900[14] (0.21 bar)
$T_{oxidation}$ [°C] (at specific P_{O2})	870–900 (TGA[49]) (0.21 bar)	<1150 (TGA[8] due to sintering) (0.21 bar)	From $T_{reductiononset}$ to >1150 (or higher, depending on dopants)
Average specific heat capacity [kJ kg^{-1} K^{-1}]	0.86 (TDcalc[18a])	0.88 (TDcalc [18a])	$CaMnO_3$ 0.82 (DSC[50]) $Ca_{0.9}Sr_{0.1}MnO_3$. 0.86 (TDcalc[18a]) $CaAl_{0.2}Mn_{0.8}O_3$ 0.918 (DSC[23])
Sensible heat 400–1000 °C [kJ kg^{-1}]	516	528	516
Reduction enthalpy [kJ kg^{-1}]*	844 (TDcalc[3]) 576 (DSC[47]) 490–550 (pilot unit[28])	267 (TDcalc[18a]) 170–200 (DSC[8]) 271 (DSC[32b])	$CaMnO_3$ 272 (P_{O2} = 0.008 bar; T = 1100 °C, TGA[17a]) 240 (Pure N_2 atmosphere, T = 1000 °C, TGA)[17c] $Ca_{0.9}Sr_{0.1}MnO_3$ 455 (P_{O2} = 0.0001 bar, T = 1000 °C, TDcalc)[15b]

TDcalc meaning "value from thermodynamic calculations," DSC meaning "values measured experimentally via Differential Scanning Calorimetry"; * "kg^{-1}" meaning "per kg of redox oxide in its oxidized state as in LHS of reaction schemes above".

© 2022 The Authors. Advanced Energy Materials published by Wiley-VCH GmbH

whereas for the (Mn,Fe)O system in particular depend also on the Fe/Mn ratio; thus typical value ranges are provided where possible. Furthermore, a direct comparison among perovskite compositions studied in the literature is difficult since on the one hand not only the extent of reduction and consequent enthalpy effects depend on the particular temperature and partial pressure of oxygen reached at the end of the heating step but also the sensible contribution is calculated over different temperature ranges. An issue to be stressed is that reaction enthalpies obtained in small-scale TGA systems, are not necessarily reproduced in larger-scale ones. An exemplary case is that of Co_3O_4/CoO pair, where on the one hand such deviations from the theoretical reaction enthalpy were proved to occur due to additional reactions accompanied by heat effects that take place during heating/cooling like the Co^{+3} spin state change, not taken care of in the theoretical calculations.[47] On the other hand, the effective reaction enthalpy (ignoring sensible contributions) calculated from measurements on the 90 kg unit mentioned above,[28] was found to range between 490 and 550 kJ kg^{-1}, i.e., approximately 60% to 70% of the theoretical value calculated from thermodynamics. This demonstrates the importance of large-scale experiments targeted on materializing the heat effects of the redox reactions into clearly identifiable and measurable temperature differences of the air HTF stream during discharging, especially with systems less exothermic than Co_3O_4/CoO like perovskites, for which the, sometimes high theoretically predicted values have yet to be demonstrated in real-application operation demonstration.

A further issue with TGA/DSC studies performed in the context described above (i.e., to screen materials compositions, determine equilibrium values and produce P–T-δ relationships) is that the heating/cooling rates usually employed (like the 5 °C min^{-1} herein) are much lower than those to be eventually encountered in real on-sun operation under intense solar flux. Such low TGA/DSC ramp rates are utilized to ensure equilibrium during heating and cooling; for example, a heating rate of 10 °C min^{-1} (combined with low oxygen partial pressures) was found too rapid to allow for equilibrium,[17a] resulting in irreversible decomposition of $CaMnO_3$ to $CaMn_2O_4$ and Ca_2MnO_4, and eventually experiments under 5 °C min^{-1} were performed for such calculations.[17a] Thus, especially when dealing with monolithic redox structures, experiments under higher, close-to-realistic heating cooling rates are of significant value to determine eventual applicability of such structures in real solar plants. In a previous work[48] we have tested similar foam specimens made of $(Mn,Fe)_2O_3$ (one of the two "competitor" materials versus which $CaMnO_3$ is compared herein) in an IR furnace under heating/cooling rates spanning between 100 and 310 °C min^{-1} and observed absolutely no evidence of macro- or microcracking on the foams (via optical microscopy and SEM respectively) even under this intense heating/cooling cycling. Despite this encouraging result, naturally, the thermomechanical performance of such foams is composition- and preparation-process-specific, depending also on factors like sintering temperature and porosity; thus, similar experiments with $CaMnO_3$ foams are also in schedule.

In previous relevant works,[27b,36] we discussed issues relevant to the reaction enthalpy of a solid storage material (in kJ kg^{-1}) that is usually employed as criterion for screening material compositions. From the industrially relevant TCS point of view however, a comparison with respect to volumetric energy storage densities (in kWh m^{-3}) and storage system volume required per stored energy unit (m^3 MW h^{-1}) seems more appropriate. These properties can be easily calculated for a specific reactor configuration, from the reaction enthalpy mentioned above and the mass of the redox oxide within the (known) reactor volume. We also performed such comparative estimates among the various structures employed in that series of studies (honeycombs, foams, pellets) using Co_3O_4 as a reference redox material (due to its high reaction enthalpy), which demonstrated that porous structures coated with a significant amount of redox oxide, or, even better, made entirely out of it, exhibit much lower value of volume required per stored energy unit than that of, e.g., the sensible-only system of Solar Tower Juelich made of porous alumina porcelain honeycombs.[27b] Alternatively, in a packed bed reactor of known volume containing a specific mass of particles, usually a particle packing density around 0.6 is assumed to convert the mass storage density (in kJ kg^{-1}) to volumetric one (in kJ m^{-3} of reactor). We followed this approach in a more recent study, exploring the concept of particle receivers for hybrid sensible-TCS with similar redox oxides in the temperature range 400–1000 °C. The case of a solar thermal power plant with a nominal power of 125 MWe and a storage capacity of 12 h was analyzed, in comparison to the use of inert commercial bauxite particles (sensible-only storage) as reference. Even though based on several simplifications, the analysis therein has concluded that, from the thermophysical data point of view, cobalt oxide is clearly advantageous, leading to significantly reduced storage mass and quite small storage volume. However, due to its high cost is unattractive compared to sensible-only reference storage on achieving the same levelized cost of electricity (LCOE) value.

Furthermore, as demonstrated in the present work, such Co_3O_4-made structures exhibit severe chemical expansion issues upon cyclic redox operation that will render them non-suitable for large-scale deployment and so do—even though much less severely—$(Mn,Fe)_2O_3$ ones. On the other hand, perovskites such as $CaMnO_3$ do not have reduction enthalpy as high as that of Co_3O_4, but, nevertheless, possess a number of other favorable attributes like the initiation of their reduction at lower temperature, significant sensible storage contribution within an ambient-to-high-temperature operation span,[18a] reversible thermal phenomena associated with phase changes that can also be exploited within that operation temperature span and, last but not least, porous structures made out of them exhibit dimensional stability upon redox cycling; in fact this last attribute is unique among the oxide material compositions studied so far for the same application. Thus, such perovskites-made porous structures could offer a pragmatic, scalable, inexpensive, and nontoxic solution for hybrid sensible-TCS systems and are worthy of further investigation and scale-up for eventual on-field demonstration. Such imminent issues of investigation in our work concern among others optimization of the foams' pore structure characteristics both at the macro- and the micro-level, i.e., preparation of foam specimens of different ppi and comparative characterization with respect to their redox performance and mechanical strength, monitoring of any porosity and pore size distribution change as a result of extensive cyclic operation (indeed, these properties were found to change in the case of cobalt-oxide-made foams with increasing

© 2022 The Authors. Advanced Energy Materials published by Wiley-VCH GmbH

16146840, 2022, 10, Downloaded from https://onlinelibrary.wiley.com/doi/10.1002/aenm.202102882 by Dtsch Zentrum F. Luft-U. Raum Fahrt In D. Helmholtz Gemein., Wiley Online Library on [05/12/2022]. See the Terms and Conditions (https://onlinelibrary.wiley.com/terms-and-conditions) on Wiley Online Library for rules of use; OA articles are governed by the applicable Creative Commons License

number of cycles[27b]) and, needless to say, extension of cyclic redox tests to a much higher number of cycles to ensure that the herein demonstrated dimensional stability can be maintained for industrial-relevant operating lifetimes.

It has to be stressed that with respect to scalability, even though in the present study RPCs (ceramic foams) were manufactured and tested, the specific approach on thermochemical energy storage should be construed within the more generic framework of "structured porous ceramics" in general rather than in the narrower "sub-category" of ceramic foams in particular. Structured porous ceramics explored in solar thermochemical applications made entirely out of redox oxides so far include ceria foams,[12] extruded zirconia-iron oxide[51] and nickel ferrite honeycombs[52] and "ordered" 3-D printed porous structures made of nickel ferrite,[52] ceria[53] and cobalt ferrite/yttria-stabilized-zirconia composites in previous works of Sandia National Laboratories, USA via "robocasting".[54] To the best of the authors' knowledge, the present work is the first in the relevant field demonstrating applications of porous structures entirely made of perovskites. Should a perovskite composition like, e.g., the one investigated here, demonstrate favorable thermomechanical characteristics like fully reversible expansion/contraction for a very large number of cycles, its scaled-up manufacturing into porous structures can take advantage of already industrially scaled shaping techniques like extrusion (employed for the production of honeycomb automotive catalytic converter substrates among others) or additive manufacturing ones like 3-D printing. Ceramic foams of large dimensions are also already produced by several companies. In this perspective, the introduction of dopants to improve the phase stability or other properties like, e.g., oxygen uptake/release, enthalpy of reaction, or mechanical rigidity of the perovskite composition can be easily implemented in the powder synthesis step from solid oxide precursors at any scale.

6. Conclusion

The eventual deployment of redox oxide-based thermochemical storage components in real-size CSP plants depends to a large extent on whether such materials can be produced cost-effectively at large-scale, but, most crucially, on whether such concepts can eventually compete with current industrial-scale sensible-only-storage, generally implemented with inexpensive systems, to justify the introduced plant complexity. Competitive advantages of the redox oxide TCS systems are the demonstration of their facile hybridization with current state-of-the-art sensible heat storage/recovery approaches, as well as the eventual performance of functionalities currently not possible with conventional sensible-only storage systems.

In this context, the present work concerned the manufacture of reticulated porous structures (foams) out of earth-abundant, noncritical-elements-based perovskite compositions and their first testing according to thermochemical storage-relevant applications and protocols. A procedure was developed for the reproducible synthesis of single-phase perovskite powder via scalable routes and the powder's necessary pre-processing for the preparation of foams. Through parametric studies on the composition of the ceramic slurries, foams made entirely of $CaMnO_3$ perovskite were manufactured in a variety of lab-scale dimensions. The foams exhibited satisfactory mechanical strength to be safely handled.

Smaller-size foams were tested for 46 reduction/oxidation cycles between 300 and 1100 °C under air in a TGA device, demonstrating constant and reproducible oxygen loss/gain without any visible deterioration of their structural integrity. In complete accordance with respect to temperatures where weight changes take place, experiments with the $CaMnO_3$ powder under the same schedule demonstrated that within the temperature range spanned, phase transformation of the orthorhombic to the cubic phase takes place upon reduction. This phase transformation was demonstrated to be fully reversible. This reversible phase transformation does not interfere with the macroscopic structural integrity of the foam and is accompanied by enthalpy effects that can be exploited to increase the storage capacity of a TCS system manufactured from such foams.

Most importantly, comparative dilatometry experiments under the same cyclic conditions with sintered rods of the same material, demonstrated that even though such specimens exhibit a length increase of ≈2% during heating, this expansion is fully relaxed during cooling. Even though this behavior is so far tested for only up to five cycles, it is nevertheless remarkable and unique compared to these of the Co_3O_4 and $(Mn,Fe)_2O_3$ redox oxide "state-of-the-art" systems considered for similar applications. These two systems exhibit very high and small, yet non-negligible, permanent "expansion" respectively upon reduction, which is progressively accumulated after each cycle. Subjected of course to further verification for a much higher number of cycles, this unique feature renders the particular $CaMnO_3$ perovskite composition very attractive for the manufacture of such porous structured objects, targeted for applications relevant to repetitive long-term redox cycling. It should also be especially considered that this full dimensional reversibility was demonstrated with "denser," sintered bar specimens of low porosity and that the inherently "open" structure of the foams and their large void space can reversibly accommodate and "buffer" any volume expansion in the macro-scale. In addition, the low cost, earth abundance, and environment-neutral character of the constituting elements is a crucial benefit of these perovskite materials.

These attributes can open a much broader perspective for the introduction of such all-perovskite-made RPCs in a variety of cyclic thermochemical processes, either directly coupled to concentrated solar irradiation or in other areas of high-temperature chemical industry involving gas-solid reactions. Particular advantages are evident in processes handling high pressure gaseous streams, due to the well-known advantageous pressure drop characteristics of RPCs relevant to other solid configurations like, e.g., particle packed beds.[55] Our current research efforts, in addition to ensuring structural integrity for a much higher number of cycles and manufacture of larger-scale specimens that can be tested in pilot-scale TCS units, concern such possible applications.

7. Experimental Section

Powder Synthesis: The experimental approach concerned at first the development of a standardized procedure for reliable and reproducible synthesis of the $CaMnO_3$ perovskite powder quantities necessary for the

© 2022 The Authors. Advanced Energy Materials published by Wiley-VCH GmbH

16146840, 2022, 10, Downloaded from https://onlinelibrary.wiley.com/doi/10.1002/aenm.202102882 by Dtsch Zentrum F. Luft-U. Raum Fahrt In D. Helmholtz Gemein., Wiley Online Library on [05/12/2022]. See the Terms and Conditions (https://onlinelibrary.wiley.com/terms-and-conditions) on Wiley Online Library for rules of use; OA articles are governed by the applicable Creative Commons License

preparation of slurries and the eventual manufacture of the $CaMnO_3$ foams, i.e., of the order of few kgs. Therefore, the $CaMnO_3$ powder was synthesized via a solid-state reaction between $CaCO_3$ (Merck, Darmstadt, Germany) and Mn_3O_4 (ERACHEM, Saint-Ghislain, Belgium) selected as inexpensive raw materials, both of purity higher than 98.0%.

While a solid-state synthesis allows the production of much larger quantities compared to the sol-gel based Pechini method, it has to be ensured that the products from different batches are single-phase $CaMnO_3$. Considering the reduced reactivity of Mn_3O_4 compared to the frequently used, but more expensive, Mn_2O_3, the fact that $CaMnO_3$ is known to decompose to a $CaMn_2O_4$ spinel and a Ca_2MnO_4 Ruddlesden-Popper phase under reducing atmosphere (low oxygen partial pressure) and high temperatures[45b,56] and the scalability of the synthesis procedure, a one-step firing with prior wet-mixing was carried out. Stoichiometric amounts of the precursors were mixed in a 1:2 wt-ratio in isopropanol and vigorously stirred for 2 h. The solids were filtered and dried for 24 h at room temperature and 24 h at 80 °C. The dried powder mixture was then fired in alumina crucibles in a Carbolite RHF 14/35 muffle furnace for 24 h at 1200 °C and heating rates of 5 °C min^{-1}. This procedure yields a product of equal high quality as the multi-step synthesis process reported in the previous relevant works.[16,41]

Foam Preparation: The foams were manufactured via the polyurethane (PU) foam replica method[57] which involves impregnation of "sacrificial" PU foam templates with slurries of the powder and subsequent drying and firing of the green body. Given this approach, the final particle size of the redox powder has to be fine enough to facilitate its formulation in stable slurries that do not settle under gravity. Therefore, the sintered powder was dry-milled in a planetary ball mill (Fritsch Pulverisette 6) with zirconia spheres as the grinding media. Various milling conditions were explored. The powders' particle size distribution (PSD) after milling was measured with a Malvern Mastersizer 2000 Low Angle Laser Light Scattering Analyzer and their specific surface area was determined with a ThermoFisher Scientific Porotec Surfer Nitrogen porosimeter. An average particle size of 5 µm was targeted for slurry production (Figure S1b in the Supporting Information). A synthetic polyelectrolyte with the commercial name DOLAPIX CE64 (supplied by Zschimmer & Schwarz GmbH & Co, Lahnstein, Germany) was employed as a dispersant to induce slurry stabilization. Slurries of the $CaMnO_3$ powder with 80%wt solid content, 17%wt water and 3%wt dispersing agent were prepared. PU foam specimens of 30 and 60 ppi were sectioned from larger samples with the commercial name Regicell 30 (FoamPartner GmbH, Leverkusen, Germany). Under stirring, the selected amount of powder was slowly added in the corresponding amount of deionized water, followed by the dispersant. After about ten minutes the temperature of the slurry was raised to 60 °C. Stirring at this temperature was continued for ten more minutes. If foaming occurred, several drops of the antifoaming agent Kontraspum KWE (supplied by Zschimmer & Schwarz GmbH & Co, Lahnstein, Germany) were added. Then, the PU specimens were impregnated in the slurries. The loaded specimens were withdrawn and excess slurry was removed by compression and a compressed air jet. The resulting green bodies were dried at ambient temperature overnight, placed on alumina tiles, and fired at 1350 °C in a single-stage sintering schedule for 3 h with a heating rate of 1 °C min^{-1} and subsequent cooling to ambient temperature with a cooling rate of 2 °C min^{-1}.

Structural Characterization: The porosity and pore size distribution of foam specimens were measured via mercury porosimetry and the specific surface area and the meso- and micropores' size distribution of powder and foam specimens via nitrogen porosimetry (Porotec Pascal 140–440 Hg porosimeter/Porotec Surfer nitrogen porosimeter respectively, both from ThermoFisher Scientific, Haan, Germany).

Phase composition characterization by X-ray diffraction (XRD) was performed with a D8-Advance (Bruker, Co-X-ray tube, Lynxe-EyeXET-Detector) diffractometer in a θ–2θ scan of the diffraction angle (2θ) 10–100° with a step size of 0.02° and 2 s per step. In situ high-temperature XRD (HT-XRD) experiments were performed on the $CaMnO_3$ powder employed for the preparation of the foams, with a D8-Advance (Bruker, Cu-X-ray tube, Lynxe-Eye XET detector) diffractometer. The specimen was heated from ambient temperature to 1300 °C and cooled again to ambient temperature under air with a ramp rate of 5°C min^{-1}; XRD spectra were obtained at 25, 500, 870, 900, 930, and 1100 °C during heat-up and cool-down in θ–2θ scans with a diffraction angle (2θ) range of 22–85°, a step size of 0.02° and 1 s per step. Heating and cooling took place with 5 °C min^{-1} and isothermal steps were included while performing the scans.

Microstructural observations of the specimens by scanning electron microscopy (SEM) were performed with a ZEISS ULTRA 55 FEG (Karl Zeiss, Oberkochen, Germany) instrument coupled with an INCA Pentafet x3 EDS X-ray microanalysis system from Oxford Instruments.

Mechanical Strength Tests: Tests were performed on 10 mm height × 20 mm diameter foam specimens, with a Dynamometer PCE-DFG N 50K device (Meschede, Germany). The specimens were clamped between two aluminum blocks, each with a mass of 49 g and compressed until rupture. The applied force was recorded as a function of time via a force gauge with a measuring accuracy of 0.1 N.

Thermogravimetric Analysis: The cyclic redox behavior of the $CaMnO_3$ foam specimens was examined by thermogravimetric analysis (TGA) experiments which were performed under air flow using a Netzsch STA 449 F3 Jupiter instrument. Based on extensive previous results with respective perovskite powders, the experimental protocol adopted did not involve any dwell at specific temperature plateaus. All samples were cycled under air atmosphere, between an upper and a lower temperature limit of 1100–300 °C respectively, with 5 °C min^{-1} heating/cooling rate, for five cycles; selected samples were cooled down in the last step under Argon. Additional runs of 5 and 12 cycles were performed on a foam sample under identical conditions. Purging was applied well before initiating thermal analysis to efficiently control the sample environment within the instrument's furnace. In addition, buoyancy corrections were carried out through blank measurements.

Dilatometry Cyclic Testing: For the dilatometry experiments, rectangular bar specimens of 10 × 5 × 5 mm were employed in a contactless optical dilatometer (L74/HS/1600, Linseis, Selb, Germany) as per the configuration shown in Figure S3 (Supporting Information). These specimens were sectioned from larger bars (Figure S3b, Supporting Information), that were prepared by uniaxial cold compression of the same, single-phase, grinded $CaMnO_3$ powder employed for the preparation of foams, in a laboratory PERKIN-ELMER hydraulic press applying a force of 5×10^4 N and subsequently sintered in the same muffle furnace utilized for synthesis and sintering of the foam specimens at 1350 °C for 20 h, similar to prior conducted studies.[41] Comparative dilatometry experiments were also performed with specimens of two other redox oxide systems employed for thermochemical storage of solar heat, namely Co_3O_4 and $(Mn,Fe)_2O_3$ since these redox oxides were comparatively tested in a TGA/DSC system with respect to their weight changes and the respective heat effects versus a range of perovskite compositions including $CaMnO_3$ in the aforementioned recent work.[41] For these two oxides, parallelepiped bar specimens were sectioned from pellets (Figure S3c, Supporting Information) sintered at 1000 °C and 1450 °C respectively. The characteristics of the dilatometry specimens are summarized in Table S1 (Supporting Information). Dilatometry experiments were carried out under air atmosphere and an identical 5-cycles heating/cooling protocol as the one employed in the TGA 5-cycles experiments was applied for comparability.

Supporting Information

Supporting Information is available from the Wiley Online Library or from the author.

Acknowledgements

This work was supported by the European Commission through the project: Perovskites as "oxygen-carriers" in solar-powered

© 2022 The Authors. Advanced Energy Materials published by Wiley-VCH GmbH

16146840, 2022, 10, Downloaded from https://onlinelibrary.wiley.com/doi/10.1002/aenm.202102882 by Dtsch Zentrum F. Luft-U. Raum Fahrt In D. Helmholtz Gemein., Wiley Online Library on [05/12/2022]. See the Terms and Conditions (https://onlinelibrary.wiley.com/terms-and-conditions) on Wiley Online Library for rules of use; OA articles are governed by the applicable Creative Commons License

redox processes for synthetic fuels production and energy storage (PERFECTION), in the framework of the EU-ERANETMED2-72-379 Call.

Open access funding enabled and organized by Projekt DEAL.

Conflict of Interest

The authors declare no conflict of interest.

Data Availability Statement

Research data are not shared.

Keywords

calcium manganate, chemical expansion, concentrated solar energy, perovskites, redox oxide pairs, reticulated porous ceramics, thermochemical energy storage

Received: September 16, 2021
Revised: January 7, 2022
Published online: January 22, 2022

[1] T. Nakamura, *Sol. Energy* **1977**, *19*, 467.
[2] W. C. Chueh, C. Falter, M. Abbott, D. Scipio, P. Furler, S. M. Haile, A. Steinfeld, *Science* **2010**, *330*, 1797.
[3] B. Wong, *Thermochemical Heat Storage for Concentrated Solar Power*, USDOE, San Diego, CA http://www.osti.gov/scitech/biblio/1039304/ (accessed: October 2011).
[4] J. Vieten, B. Bulfin, F. Call, M. Lange, M. Schmücker, A. Francke, M. Roeb, C. Sattler, *J. Mater. Chem. A* **2016**, *4*, 13652.
[5] Y. Lu, L. Zhu, C. Agrafiotis, J. Vieten, M. Roeb, C. Sattler, *Prog. Energy Combust. Sci.* **2019**, *75*, 100785.
[6] B. Bulfin, J. Vieten, C. Agrafiotis, M. Roeb, C. Sattler, *J. Mater. Chem. A* **2017**, *5*, 18951.
[7] A. J. Carrillo, J. González-Aguilar, M. Romero, J. M. Coronado, *Chem. Rev.* **2019**, *119*, 4777.
[8] A. J. Carrillo, D. P. Serrano, P. Pizarro, J. M. Coronado, *ChemSusChem* **2015**, *8*, 1947.
[9] S. M. Babiniec, E. N. Coker, J. E. Miller, A. Ambrosini, *Sol. Energy* **2015**, *118*, 451.
[10] D. A. Dimitrakis, N. I. Tsongidis, A. G. Konstandopoulos, *Phys. Chem. Chem. Phys.* **2016**, *18*, 23587.
[11] M. Kubicek, A. H. Bork, J. L. M. Rupp, *J. Mater. Chem. A* **2017**, *5*, 11983.
[12] D. Marxer, P. Furler, M. Takacs, A. Steinfeld, *Energy Environ. Sci.* **2017**, *10*, 1142.
[13] J. Vieten, B. Bulfin, P. Huck, M. Horton, D. Guban, L. Zhu, Y. Lu, K. A. Persson, M. Roeb, C. Sattler, *Energy Environ. Sci.* **2019**, *12*, 1369.
[14] S. M. Babiniec, E. N. Coker, J. E. Miller, A. Ambrosini, *Int. J. Energy Res.* **2016**, *40*, 280.
[15] a) J. E. Miller, A. Ambrosini, S. M. Babiniec, E. N. Coker, C. K. Ho, H. Al-Ansary, S. M. Jeter, P. G. Loutzenhiser, N. G. Johnson, E. B. Stechel, in *ASME 2016 10th Int. Conf. on Energy Sustainability Collocated with the ASME 2016 Power Conf. and the ASME 2016 14th Int. Conf. on Fuel Cell Science, Engineering and Technology*, ASME, New York **2016**, pp. V001T004A024; b) L. Imponenti, K. J. Albrecht, J. W. Wands, M. D. Sanders, G. S. Jackson, *Sol. Energy* **2017**, *151*, 1; c) L. Imponenti, K. J. Albrecht, R. Kharait, M. D. Sanders, G. S. Jackson, *Appl. Energy* **2018**, *230*, 1; d) A. Ambrosini, J. E. Miller, D. D. Gill, *US Patent 10107268*, **2018**.
[16] M. Pein, C. Agrafiotis, J. Vieten, D. Giasafaki, S. Brendelberger, M. Roeb, C. Sattler, *Sol. Energy* **2020**, *198*, 612.
[17] a) E. Mastronardo, X. Qian, J. M. Coronado, S. M. Haile, *J. Mater. Chem. A* **2020**, *8*, 8503; b) F. Jin, C. Xu, H. Yu, X. Xia, F. Ye, X. Li, X. Du, Y. Yang, *ACS Appl. Mater. Interfaces* **2021**, *13*, 3856; c) D. Yilmaz, E. Darwish, H. Leion, *Ind. Eng. Chem. Res.* **2021**, *60*, 1250; d) K. J. Albrecht, G. S. Jackson, R. J. Braun, *Sol. Energy* **2018**, *167*, 179; e) E. Mastronardo, X. Qian, J. M. Coronado, S. M. Haile, *J. Energy Storage* **2021**, *40*, 102793.
[18] a) G. S. Jackson, L. Imponenti, K. J. Albrecht, D. C. Miller, R. J. Braun, *J. Sol. Energy Eng.* **2019**, *141*, 021016; b) N. Siegel, M. Gross, C. Ho, T. Phan, J. Yuan, *Energy Procedia* **2014**, *49*, 1015.
[19] a) M. Neises, S. Tescari, L. de Oliveira, M. Roeb, C. Sattler, B. Wong, *Sol. Energy* **2012**, *86*, 3040; b) E. Alonso, C. Pérez-Rábago, J. Licurgo, E. Fuentealba, C. A. Estrada, *Sol. Energy* **2015**, *115*, 297; c) S. Tescari, P. Sundarraj, G. Moumin, J. P. R. Duarte, C. Agrafiotis, L. de Oliveira, C. Willsch, M. Roeb, C. Sattler, *AIP Conf. Proc.* **2020**, *2303*, 140007.
[20] a) S. Á. De Miguel, J. Gonzalez-Aguilar, M. Romero, *Energy Procedia* **2014**, *49*, 676; b) G. Flamant, D. Gauthier, H. Benoit, J.-L. Sans, R. Garcia, B. Boissière, R. Ansart, M. Hemati, *Chem. Eng. Sci.* **2013**, *102*, 567; c) B. Wang, L. Li, F. Schäfer, J. J. Pottas, A. Kumar, V. M. Wheeler, W. Lipiński, *Chem. Eng. J.* **2021**, *412*.
[21] A. J. Schrader, A. P. Muroyama, P. G. Loutzenhiser, *Sol. Energy* **2015**, *118*, 485.
[22] H. E. Bush, P. G. Loutzenhiser, *Sol. Energy* **2018**, *174*, 617.
[23] A. J. Schrader, G. L. Schieber, A. Ambrosini, P. G. Loutzenhiser, *Appl. Therm. Eng.* **2020**, *173*, 115257.
[24] A. Ambrosini, J. E. Miller, S. M. Babiniec, P. Loutzenhiser, E. B. Stechel, S. Jeter, H. Al-Ansary, *High Performance Reduction/Oxidation Metal Oxides for Thermochemical Energy Storage (PROMOTES): A Project Overview*, SAND2018-7073C, Sandia National Lab. (SNL-NM), Albuquerque, NM, **2018**
[25] a) A. Glück, R. Tamme, H. Kalfa, C. Streuber, *Sol. Energy Mater.* **1991**, *24*, 240; b) D. C. Stack, D. Curtis, C. Forsberg, *Appl. Energy* **2019**, *242*, 782.
[26] S. Zunft, M. Hänel, M. Krüger, V. Dreißigacker, F. Göhring, E. Wahl, *J. Sol. Energy Eng.* **2011**, *133*, 031019.
[27] a) C. Pagkoura, G. Karagiannakis, A. Zygogianni, S. Lorentzou, M. Kostoglou, A. G. Konstandopoulos, M. Rattenburry, J. W. Woodhead, *Sol. Energy* **2014**, *108*, 146; b) C. Agrafiotis, S. Tescari, M. Roeb, M. Schmücker, C. Sattler, *Sol. Energy* **2015**, *114*, 459; c) G. Karagiannakis, C. Pagkoura, E. Halevas, P. Baltzopoulou, A. G. Konstandopoulos, *Sol. Energy* **2016**, *133*, 394; d) C. Agrafiotis, A. Becker, M. Roeb, C. Sattler, *Sol. Energy* **2016**, *139*, 676.
[28] S. Tescari, A. Singh, C. Agrafiotis, L. de Oliveira, S. Breuer, B. Schlögl-Knothe, M. Roeb, C. Sattler, *Appl. Energy* **2017**, *189*, 66.
[29] D. Xiang, C. Gu, H. Xu, G. Xiao, *Small* **2021**, *17*, 2101524.
[30] S. Ströhle, A. Haselbacher, Z. R. Jovanovic, A. Steinfeld, *Appl. Energy* **2017**, *196*, 51.
[31] S. Ströhle, A. Haselbacher, Z. R. Jovanovic, A. Steinfeld, *Energy Environ. Sci.* **2016**, *9*, 1375.
[32] a) M. Wokon, T. Block, S. Nicolai, M. Linder, M. Schmücker, *Sol. Energy* **2017**, *153*, 471; b) M. Wokon, A. Kohzer, M. Linder, *Sol. Energy* **2017**, *153*, 200; c) N. C. Preisner, T. Block, M. Linder, H. Leion, *Energy Technol.* **2018**, *6*, 2154.
[33] M. Gigantino, S. Sas Brunser, A. Steinfeld, *Energy Fuels* **2020**, *34*, 16772.
[34] a) A. Atkinson, T. Ramos, *Solid State Ionics* **2000**, *129*, 259; b) N. Knoblauch, H. Simon, M. Schmücker, *Solid State Ionics* **2017**, *301*, 43.
[35] C. L. Muhich, *J. Phys. Chem. C* **2017**, *121*, 8052.
[36] C. Agrafiotis, T. Block, M. Senholdt, S. Tescari, M. Roeb, C. Sattler, *Sol. Energy* **2017**, *149*, 227.

© 2022 The Authors. Advanced Energy Materials published by Wiley-VCH GmbH

16146840, 2022, 10, Downloaded from https://onlinelibrary.wiley.com/doi/10.1002/aenm.202102882 by Dtsch Zentrum F. Luft-U. Raum Fahrt In D. Helmholtz Gemein., Wiley Online Library on [05/12/2022]. See the Terms and Conditions (https://onlinelibrary.wiley.com/terms-and-conditions) on Wiley Online Library for rules of use; OA articles are governed by the applicable Creative Commons License

[37] D. M. Beall, W. A. Cutler, *Am. Ceram. Soc. Bull.* **2020**, *99*, 24.
[38] a) S. Funayama, H. Takasu, M. Zamengo, J. Kariya, S. T. Kim, Y. Kato, *Energy Storage* **2019**, *1*, e53; b) S. Funayama, H. Takasu, S. T. Kim, Y. Kato, *Energy* **2020**, *201*, 117673.
[39] T. Fey, U. Betke, S. Rannabauer, M. Scheffler, *Adv. Eng. Mater.* **2017**, *19*, 1700369.
[40] A. M. Parvanian, H. Salimijazi, M. Shabaninejad, U. Troitzsch, P. Kreider, W. Lipiński, M. Saadatfar, *RSC Adv.* **2020**, *10*, 23049.
[41] C. Agrafiotis, M. Pein, D. Giasafaki, S. Tescari, M. Roeb, C. Sattler, *J. Sol. Energy Eng.* **2019**, *141*, 021010.
[42] M. Pishahang, Y. Larring, M. McCann, R. Bredesen, *Ind. Eng. Chem. Res.* **2014**, *53*, 10549.
[43] a) E. S. Reddy, J. Noudem, C. Goupil, *Energy Convers. Manage.* **2007**, *48*, 1251; b) J. Noudem, S. Lemonnier, M. Prevel, E. Reddy, E. Guilmeau, C. Goupil, *J. Eur. Ceram. Soc.* **2008**, *28*, 41.
[44] A. R. Studart, U. T. Gonzenbach, E. Tervoort, L. J. Gauckler, *J. Am. Ceram. Soc.* **2006**, *89*, 1771.
[45] a) H. Taguchi, M. Nagao, T. Sato, M. Shimada, *J. Solid State Chem.* **1989**, *78*, 312; b) E. I. Leonidova, I. A. Leonidov, M. V. Patrakeev, V. L. Kozhevnikov, *J. Solid State Electrochem.* **2011**, *15*, 1071.
[46] R. Buck, C. Agrafiotis, S. Tescari, N. Neumann, M. Schmücker, *Front. Energy Res.* **2021**, *9*, 694248.
[47] T. Block, M. Schmücker, *Sol. Energy* **2016**, *126*, 195.
[48] C. Agrafiotis, S. Tescari, M. Roeb, C. Sattler, *AIP Conf. Proc.* **2018**, *2033*, 100001.
[49] C. Agrafiotis, M. Roeb, M. Schmücker, C. Sattler, *Sol. Energy* **2014**, *102*, 189.
[50] P. Thiel, J. Eilertsen, S. Populoh, G. Saucke, M. Döbeli, A. Shkabko, L. Sagarna, L. Karvonen, A. Weidenkaff, *J. Appl. Phys.* **2013**, *114*, 243707.
[51] L. S. Walker, J. E. Miller, G. E. Hilmas, L. R. Evans, E. L. Corral, *Energy Fuels* **2012**, *26*, 712.
[52] a) S. Lorentzou, C. Pagkoura, A. Zygogianni, G. Karagiannakis, A. Konstandopoulos, *Int. J. Hydrogen Energy* **2017**, *42*, 19664; b) S. Lorentzou, D. Dimitrakis, A. Zygogianni, G. Karagiannakis, A. Konstandopoulos, *Sol. Energy* **2017**, *155*, 1462.
[53] M. Hoes, S. Ackermann, D. Theiler, P. Furler, A. Steinfeld, *Energy Technol.* **2019**, *7*, 1900484.
[54] a) R. B. Diver, J. E. Miller, M. D. Allendorf, N. P. Siegel, R. E. Hogan, *J. Sol. Energy Eng.* **2008**, *130*, 41001; b) J. E. Miller, M. D. Allendorf, R. B. Diver, L. R. Evans, N. P. Siegel, J. N. Stuecker, *J. Mater. Sci.* **2008**, *43*, 4714.
[55] M. V. Twigg, J. T. Richardson, *Ind. Eng. Chem. Res.* **2007**, *46*, 4166.
[56] E. Bakken, T. Norby, S. Stølen, *Solid State Ionics* **2005**, *176*, 217.
[57] M. Scheffler, P. Colombo, *Cellular Ceramics: Structure, Manufacturing, Properties and Applications*, John Wiley & Sons, New York **2006**.

© 2022 The Authors. Advanced Energy Materials published by Wiley-VCH GmbH

16146840, 2022, 10, Downloaded from https://onlinelibrary.wiley.com/doi/10.1002/aenm.202102882 by Dtsch Zentrum F. Luft-U. Raum Fahrt In D. Helmholtz Gemein., Wiley Online Library on [05/12/2022]. See the Terms and Conditions (https://onlinelibrary.wiley.com/terms-and-conditions) on Wiley Online Library for rules of use; OA articles are governed by the applicable Creative Commons License